# Development of a Two-Dimensionally Tunable Focusing Monochromator for Protein Crystallography at High-Energy Undulator Beamlines

by

Yoshiaki Kawano

A dissertation submitted to
Division of Biological Sciences, Graduate School of Science, Hokkaido University, Sapporo 060 Japan
in partial fulfillment of the requirement for the degree of
Doctor of Science

January 1996

(1)

# Development of a Two-Dimensionally Tunable Focusing Monochromator for Protein Crystallography at High-Energy Undulator Beamlines

**by**

**Yoshiaki Kawano**

*A dissertation submitted to*

*Division of Biological Sciences, Graduate School of Science, Hokkaido University, Sapporo 060 Japan*

*in partial fulfillment of the requirement for the degree of*

*Doctor of Science*

*January 1996*

# Contents

# 1. Introduction

Protein crystal structure analysis is a powerful tool for revealing three-dimensional structures of biological macromolecules at atomic resolution. In order to collect reflection data rapidly from sample crystals and to resolve phase problems resulting from anomalous dispersion effects, synchrotron radiation with high intensity and a wide range of accessible energies is very useful in protein crystallography. In second-generation synchrotron radiation facilities, however, X-ray energies applicable to protein crystallography have been limited to below 20 keV since the bending magnets in these facilities generate X-rays with a sufficiently high flux only at energies below 20 keV. In the third-generation facilities, such as the SPring-8, high-brilliance X-rays have become available in a wide energy range of 6 - 40 keV from an in-vacuum undulator having fundamental and third-harmonic emissions. High-intensity X-rays in the region between 20 and 40 keV, which are not available in the second-generation facilities, are desired in protein crystallography since errors caused by absorption of X-rays by a protein crystal are essentially eliminated.

However, there exist no optical elements suitable for converging high-energy X-rays in horizontal and vertical directions. Total reflection mirrors cannot be used because the critical angles are so small that the radii of curvature are very large. The triangular bending monochromator must be combined with another focusing element such as a total reflection mirror in order to realize two-dimensional focusing. The sagittal focusing monochromator is, in general, used to obtain a pseudo-two-dimensional focal point. However, its application to X-rays from an undulator is not feasible since the size of the X-rays is too small for convergence using the sagittal focusing geometry. There are also various types of two-dimensional focusing

monochromators fabricated by simultaneous bending in two directions. None of these, however, are tunable in the X-ray energy range. Because tunability is an indispensable function of monochromators used in protein crystallography, these monochromators cannot accommodate the present purpose.

It is clear that reliable two-dimensionally tunable focusing monochromators must be developed in order to effectively utilize high-energy and high-intensity X-rays, that are extracted from the undulator beamlines in the third-generation facilities.

In this dissertation, a newly developed two-dimensionally tunable focusing monochromator will be described. It consists of a silicon wafer which has an oblique-cut angle between the Bragg net plane and the crystal surface and is adhered onto a tablelike copper block. The radii of curvature are varied independently in sagittal and meridional directions by expanding the spaces between the table legs. The versatilities of the meridional and sagittal curvatures were confirmed from the results of X-ray experiments and three-dimensional shape measurements, respectively. The two-dimensional focusing ability was demonstrated using high-energy X-rays of 37.7 keV emitted from a bending magnet source of the Photon Factory. A quasi-isotropic profile of converged X-rays was achieved near the focal position. The apparent gain of photon flux was 21. Owing to these excellent characteristics of the monochromator, a diffraction pattern of hen egg white lysozyme crystal was successfully obtained using high-energy X-rays.

If the present monochromator is used in the SPring-8 undulator beamline, the high-energy X-rays between 20 and 40 keV may have $10^5$ times higher intensity than that of X-rays obtained from the Photon Factory bending magnet beamline. In addition, heavy elements from cadmium to iodine are applicable to phase

determination. This monochromator will contribute much to the elucidation of the structures of biological macromolecules in the near future.

# 2. Problems in Protein Crystallography

Biological processes basically depend on structures and interactions of macromolecules (proteins, nucleic acids, and carbohydrates) in living cells. The structural and kinematical information of these macromolecules provides useful clues for understanding life. Among these molecules, proteins form one of the largest groups. Proteins consist of one or more polypeptide chains constructed from twenty naturally occurring amino acids. The chains are folded into a three-dimensional structure, and the structure determines chemical and physical properties as well as the resultant functions of proteins.

Recently, the tertiary structure of a protein can be determined within one year using X-ray equipment and computers with excellent performance when good-quality crystals are obtained. With recent advances in DNA sequence determination, however, studies on the primary structures of proteins have shown a 50-times increase over studies on the tertiary structures of proteins (Bowie, Luthy & Eisenberg, 1990). The determination of the DNA sequence by which the protein primary structure is elucidated is easier than the determination of the tertiary structures of proteins. In order to overcome the discrepancy in the number of studies conducted on the tertiary and primary structures of proteins, protein structure analysis by X-ray crystallography must become much easier. However, there exist some problems in protein crystallography (e.g., accurate data collection, identification of the best derivatives, phase problems, etc.).

In general, there are seven stages in the X-ray crystal structure analysis of a protein.

1. Sample preparation.
2. Crystallization.
3. Determination of unit cell parameters.
4. Measurement of X-ray diffraction intensities.
5. Solution of crystallographic phase problem.
6. Interpretation of electron density map (molecular modeling).
7. Refinement of molecular model on reflection data set.

Each stage has some difficulties. However, the number of difficulties will be markedly reduced if good-quality crystals are obtained.

## 2.1. Crystallization of proteins

Protein crystals grow from supersaturated solutions as in the case of low molecular weight compounds. The basic technique in protein crystallization is to add precipitants to a protein solution. The precipitants deprive the proteins of water molecules, and convert the protein solution into a supersaturated state. Since proteins have greater variety of properties than low molecular weight compounds, it is important to choose the best condition for crystallization. A successful condition for crystallization of a certain protein may not be applicable to other proteins. Optimization of the crystallization condition is therefore necessary to obtain good-quality crystals for X-ray structure analysis, because the crystal quality greatly affects the accuracy of the molecular model.

The main factors that affect crystal growth and the kinds of precipitants used are listed in Table 1.

Table 1 : Factors affecting crystallization

| A. factors which influence crystal growth | B. precipitants usually used in crystallization |
|---|---|
| 1. kind of buffer and pH | 1. ammonium sulfate |
| 2. ionic strength | 2. sodium citrate or ammonium citrate |
| 3. kind and concentration of precipitant | 3. potassium or sodium phosphate |
| 4. temperature and vibration in crystallization | 4. ethanol |
| 5. purity and concentration of protein solution | 5. isopropanol |
| 6. kind and concentration of additive | 6. 2-methyl-2,4-pentanediol (MPD) |
| | 7. polyethylene glycol (PEG) 1000, 4000, 8000 |

The crystallization condition of proteins whose three-dimensional structures have already been determined can be used to obtain good-quality native crystals of a similar protein. Since the crystallization conditions of many proteins have been already incorporated into a data base, such a data base can be used for determining the starting conditions for crystallization. Moreover, it is preferable to examine the crystallization conditions in consideration of heavy atom derivative preparations (several heavy atoms are insoluble in the phosphate buffer).

The crystallization techniques include batch process, vapor diffusion and microdialysis (McPherson, 1982; Michel, 1991; McPherson, 1990). In the batch process, the solution condition does not change before and after the crystallization. In contrast, the solution conditions in vapor diffusion and microdialysis change slowly into the supersaturated state. Hence, these two techniques are suitable for growing large, high-quality crystals.

A crystallization condition determination kit is available commercially (Jancarik & Kim, 1991). This kit is provided in combination with precipitants and

buffers which have high success rates in crystallization as reported so far. The kit is utilized in the search for an initial crystallization condition. In order to obtain a crystal suitable for X-ray analysis, however, the crystallization conditions determined by this method must be refined. McPherson (1990) presented a flow chart for the systematic determination of crystallization conditions. An automated equipment for crystallization (Chayen, Stewart, Maeder & Blow, 1990) is also available commercially.

## 2.2. Structural analysis of small crystal

It is difficult to grow a perfect protein crystal of appropriate size. Usually, protein crystals grow imperfectly (low resolution or insufficient reflectivity) or are very small (under 0.1 × 0.1 mm). An imperfect crystal cannot be used for X-ray structural analysis, yet a small perfect crystal can be used. Even if synchrotron radiation facilities are available as X-ray sources, crystal size of about 100 μm or more is still necessary for X-ray crystal structure analyses because diffraction intensity from the protein crystals is very weak.

In spite of the search for a variety of crystallization conditions, structure analyses of many proteins are interrupted because their crystals do not grow to a sufficient size. The crystallization of the photosystem II complex of rice has been attempted for many years in the Photosynthesis Science Laboratory of the Institute of Physical and Chemical Research (RIKEN). Needlelike crystals which gave diffraction patterns with a resolution of 12 Å were obtained several years ago (Shen, Kamiya, Han, Iwasaki & Inoue, 1994). Since the crystal thickness is less than 40 μm, concrete analysis has been unsuccessful. In the case of nitrile hydratase, crystallization of which has been undertaken in the Chemical Engineering

Laboratory of RIKEN, the size of the obtained crystals does not exceed 100 μm. Because of the weak diffraction intensity from small crystals, the research target is shifted to other crystal system with lower resolution but larger size (Nagashima, *et al.* 1995).

The X-ray structure analysis with small crystals of several tens microns in size has been attempted using the white beam Laue method (Hedman, *et al.* 1985). This method has advantages in that many diffraction spots can be recorded at once without sample rotation. However, a high-quality diffraction pattern for structural analysis cannot be obtained by the white beam Laue method due to radiation damage on sample, increase in background level from diffuse scattering and streaks of diffraction spots. Whether the small crystals have sufficient perfection for structural analysis has not been determined (Andrews, *et al.* 1987; Gonzalez & Nave, 1994). X-ray equipment with suitable optics for evaluating small-crystal perfection must be constructed.

In monochromatic X-ray diffraction experiments on the small crystals, it is necessary to suppress radiation damage on the samples and background scattering. Monochromatic X-rays should be well collimated and the optical system has to be designed more accurate than that for the experiments on usual size crystals.

If higher intensity X-rays than those obtained from existing synchrotron radiation facilities can be realized, studies on the three-dimensional structures of proteins using small crystals will be facilitated.

## 2.3. Utilization of high-energy X-rays

In order to improve the quality of diffraction data, it is preferable to obtain a complete data set from only one crystal. Brilliant beams of high-energy X-rays are preferred in protein crystallography, since the amount of radiation damage caused by incident X-rays is expected to be decreased by increasing the X-ray energy up to 40 keV, as well as by increasing the brilliance (Helliwell, 1992). The use of high-energy X-rays causes a reduction in X-ray absorption by sample crystals, as shown in Fig. 1, and the radiation damage on the crystals can be greatly reduced. It is a very attractive method for collecting diffraction data with high accuracy (Helliwell, Moore, Papiz & Smith, 1984).

## 2.4. Phase determination

The phase problem in X-ray protein crystallography must be solved in order to obtain electron density distributions from the diffraction data. The multiple isomorphous replacement method (MIR) (Crick & Magdoff, 1956) with optimized anomalous scattering (OAS) (Baker, *et al*. 1990) is used to solve the crystallographic phase problem for a new protein crystal structure. The OAS technique is based on the multiwavelength anomalous scattering method (MAD) (Hendrickson, 1991) for heavy atom derivatives.

The diffraction intensity $I(\boldsymbol{h})$ at a certain reflection index $\boldsymbol{h}$ can be written as

$$I(\boldsymbol{h}) \propto \lambda^3 LPA\left(V_c/V^2\right)F(\boldsymbol{h})^2 , \qquad (1)$$

where $F(\boldsymbol{h})$ is the structural amplitude, $\lambda$ is the X-ray wavelength, $L$ is the Lorentz factor, $P$ is the polarization factor, $A$ is the absorption factor, $V_c$ is the crystal volume and $V$ is the volume of a unit cell.

Denoting the position $xyz$ in the unit cell as the vector $\mathbf{x}$ and the electron density as $\rho(\boldsymbol{x})$, the structure factor $\boldsymbol{F}(\boldsymbol{h})$ is written as the Fourier transform of the electron density,

$$\boldsymbol{F}(\boldsymbol{h}) = V\int_0^1\int_0^1\int_0^1 \rho(\boldsymbol{x})\exp(2\pi i\boldsymbol{h}\boldsymbol{x})\,\mathrm{d}x\,\mathrm{d}y\,\mathrm{d}z\,. \tag{2}$$

The structure factor $\boldsymbol{F}(\boldsymbol{h})$ is expressed as

$$\boldsymbol{F}(\boldsymbol{h}) = F(\boldsymbol{h})\exp\{i\alpha(\boldsymbol{h})\}, \tag{3}$$

where $F(\boldsymbol{h})$ is the structural amplitude and $\alpha(\boldsymbol{h})$ is the phase angle.

The electron density is obtained from the Fourier transform of equation (3). The Fourier transform is rewritten as a summation with the indices $h,k,l$ as

$$\rho(\boldsymbol{x}) = 1/V\sum_h\sum_k\sum_l F(\boldsymbol{h})\exp(-2\pi i\boldsymbol{h}\boldsymbol{x})\,. \tag{4}$$

The structural amplitude is calculated from the measured diffraction intensity according to equation (1) but the phase angle $\alpha$ cannot be measured directly. This is the so-called phase problem. In order to calculate electron density distribution, it is necessary to obtain the phase angle.

The atomic scattering factor $f_\lambda$ at wavelength $\lambda$ is

$$f_\lambda = f^0 + f'_\lambda + if''_\lambda, \tag{5}$$

where $f^0$ is the atomic scattering factor without anomalous dispersion effects and which has no wavelength dependence, and $f'$ and $f''$ are the real and imaginary parts of the anomalous scattering factor, respectively.

The structure factor represented by equation (2) is rewritten as

$$\boldsymbol{F}(\boldsymbol{h}) = \sum_{j=1,N} f_{\lambda j} T_j \exp(2\pi i \boldsymbol{h} \boldsymbol{x}_j), \tag{6}$$

where $f_{\lambda j}$ is the atomic scattering factor of the $j$th atom, $T_j$ is the temperature effect due to heat vibration and $N$ is the number of atoms in a unit cell.

The use of equation (6) is the basic strategy for the structure analysis. When a heavy atom contributes largely to the structural amplitude the MIR method may be applied.

The atomic scattering factor depends on the wavelength. Moreover, the phase of X-rays scattered by an individual atom depends on the kind of atom and its environment (Templeton & Templeton, 1985). Such an effect of anomalous scattering can be used in the MIR for heavy atom derivatives with the OAS technique (Matthews, 1966a; Matthews, 1966b).

If an approximate electron density distribution or a tentative set of atomic coordinates is known, the phase can be calculated using expression (2) or (6). It is a classical and basic method to refine the electron density distribution or structural model using a Fourier transform.

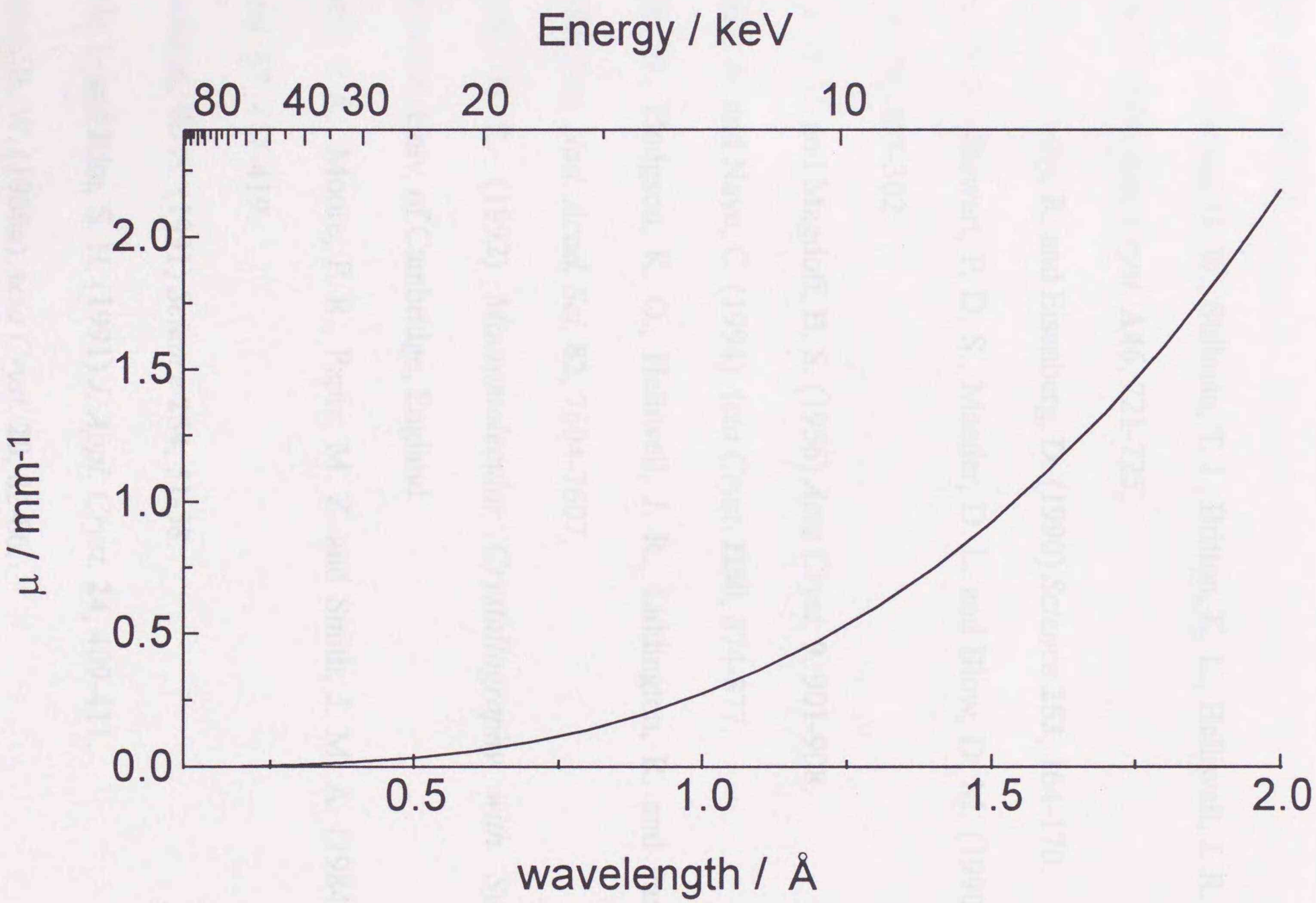


Fig. 1 : Wavelength dependence of linear absorption coefficient ($\mu$) of a standard protein crystal.

# References


Andrews, S. J., Hails, J. E., Harding, M. M. and Cruickshank, D. W. J. (1987) *Acta Cryst.* **A43**, 70-73.

Baker, P. J., Farrans, G. W., Stillman, T. J., Britton, K. L., Helliwell, J. R. and Rice, D. W. (1990) *Acta Cryst.* **A46**, 721-725.

Bowie, J. U., Luthy, R. and Eisenberg, D. (1990) *Science* **253**, 164-170.

Chayen, N. E., Stewart, P. D. S., Maeder, D. L. and Blow, D. M. (1990) *J. Appl. Cryst.* **23**, 297-302.

Crick, F. H. C. and Magdoff, B. S. (1956) *Acta Cryst.* **9**, 901-908.

Gonzalez, A. and Nave, C. (1994) *Acta Cryst.* **D50**, 874-877.

Hedman, B., Hodgson, K. O., Helliwell, J. R., Liddington, R. and Pariz, M. Z. (1985) *Pro. Natl. Acad. Sci.* **82**, 7604-7607.

Helliwell, J. R. (1992) *Macromolecular Crystallography with Synchrotron Radiation*, Univ. of Cambridge, England.

Helliwell, J. R., Moore, P. R., Papiz, M. Z. and Smith, J. M. A. (1984) *J. Appl. Cryst.* **17**, 417-419.

Hendrickson, W. A. (1991) *Science* **254**, 51-58.

Jancarik, J. and Kim, S. H. (1991) *J. Appl. Cryst.* **24**, 409-411.

Matthews, B. W. (1966a) *Acta Cryst.* **20**, 82-86.

Matthews, B. W. (1966b) *Acta Cryst.* **20**, 230-239.

McPherson, A. (1982) *Preparation and Analysis of Protein Crystals*, Wiley, New York.

McPherson, A. (1990) *Eur. J. Biochem.* **189**, 1-23.

Michel, H. (1991) *Crystallization of Membrance Proteins*, CRC Press, Boca Raton.

Nagashima, S., Nakasako, M., Kamiya, N., Odaka, M., Yohda, M., Ueki, T., Iwasaki, H. and Endo, I. (1995) 日本生物物理学会 第 33 回年会 講演予講集. pp. S10.

Shen, J.-R., Kamiya, N., Han, K.-C., Iwasaki, H. and Inoue, Y. (1994) Program and Abstracts in First East Asian Symposium on Biophysics. pp. 134.

Templeton, D. H. and Templeton, L. K. (1985) *Acta Cryst.* **A41**, 365-371.

# 3. Synchrotron Radiation Facilities and X-ray Optics

## 3.1. Synchrotron radiation facilities

Synchrotron radiation facilities are used as sources of extremely high-intensity X-rays. These X-rays were observed for the first time using a round accelerator of electrons, the electron synchrotron.

The synchrotron radiation facilities are classified into three generations as follows:

1. The first-generation facilities are parasitic in the electron synchrotrons for high-energy physics. Such facilities were used mainly for spectroscopy in the vacuum ultraviolet region in the 1960's.

2. The second-generation facilities are dedicated, and major sources are the bending magnets of storage rings. In these facilities, however, the applicability of X-ray energies in protein crystallography has been limited to below 20 keV since the bending magnets in these facilities generate sufficiently high-brilliance X-rays only at energies up to 20 keV.

3. The third-generation facilities have been constructed recently in order to produce synchrotron radiations with extremely high-brilliance X-rays using special insertion devices (Buras & Materlik, 1986; Shenoy & Moncton, 1988; JAERI-RIKEN SPring-8 Project Team, 1991) such as an undulator (Attwood, Halbach & Kim, 1985) and a multipole wiggler. These devices consist of many magnets with alternating polarity in a straight line. The undulator is capable of emitting quasi-monochromatic, high-brilliance, and low-divergence X-rays. Undulators installed in the third-generation facilities have drawn the attention of protein crystallographers

since they meet practically all the conditions necessary for X-ray protein crystallography.

SPring-8 (Super Photon ring 8 GeV) (JAERI-RIKEN SPring-8 Project Team, 1991) is a third-generation facility presently under construction in Hyogo Prefecture as a joint project of the Japan Atomic Energy Research Institute (JAERI) and the Institute of Physical and Chemical Research (RIKEN). The storage ring energy (8 GeV) is the highest in the third-generation facilities in the world. Based on its high-energy characteristics, high-brilliance X-rays will be available in a wide energy range of 6 - 40 keV from a vacuum-sealed undulator, the so-called "in-vacuum undulator" (Yamamoto, *et al*. 1992). The SPring-8 will be completed in the autumn of 1997 including the beamlines for experiments.

The undulators of SPring-8 will give X-rays of 1.84 mm × 0.92 mm area at a distance of 46 m, which is too large for protein crystallography with crystals smaller than 100 μm. On the other hand, the diffraction intensity from sample crystals decreases with increasing in X-ray energy (Equation (1) shows that the X-ray energy is inversely proportional to its wavelength.). Therefore, it is required that optical elements for use in protein crystallography with small crystals must provide small-area, high-intensity and high-energy X-rays.

This requirement is met with the use of a focusing optical element that converges X-rays while retaining the desired high intensity. The next section describes bending mirrors and bending crystal monochromators which are used as focusing optical elements for X-rays.

## 3.2. Bending mirror

The most common optical device used as a focusing element is the bending mirror. X-ray mirrors use the total reflection phenomenon.

When X-rays are focused on a material of refractive index $n$, refraction occurs at the material boundary. The relation between the refractive index $n$ and the glancing angles $\theta_1$ (for incident beam) and $\theta_2$ (for refracted beam) is given by Snell's law:

$$n = \cos\theta_1 / \cos\theta_2. \tag{7}$$

The refractive index $n$ becomes 1 - $\delta(\delta > 0)$ since $n < 1$ in the X-ray range. If the glancing angle of incident X-rays is smaller than the critical angle $\theta_c$, the X-rays will be reflected without penetration into the material and equation (7) can be re-written as

$$n = 1 - \delta = \cos\theta_2. \tag{8}$$

This is a well-known situation where total reflection occurs at an incident angle smaller than the critical angle $\theta_c$. $\delta$ in equation (8) is expressed as

$$\delta = \lambda^2 r_e \Big/ (2\pi V_c) \sum \left( Z_j + f_j' \right), \tag{9}$$

where $\lambda$ is the incident X-ray wavelength, $r_e$ is the classical electron radius, $V_c$ is the volume of a crystal unit cell, $Z_j$ is the atomic number of the $j$-th atom in the unit cell and $f_j'$ is the real part of the anomalous scattering factor.

When the mirror is made of only one material the anomalous scattering factor is disregarded and $\delta$ is

$$\delta = 2.0 \times 10^{-4} \rho / E^2, \tag{10}$$

where $\rho$ is the material density (in g/cm$^3$) and $E$ is the X-ray energy value (in keV).

In the hard X-ray region, $\delta$ is very small ($10^{-5}$ - $10^{-6}$), resulting in a small critical angle $\theta_c$ given by

$$\theta_c = (2\delta)^{1/2} = 2.0 \times 10^{-2} \rho^{1/2} / E \text{ (rad)} = 3 - 10 \text{ mrad.} \tag{11}$$

The glancing angle $\theta_i$ is also small since it should be smaller than $\theta_c$.

Equation (11) shows that the critical angle increases in proportion to the square root of the material density. Therefore, the critical angle is increased by coating the mirror surface with high-density metals such as platinum and gold. Fig. 2 shows the glancing angle dependence of the reflectivity of X-ray mirrors.

Expression (11) also indicates that the critical angle is inversely proportional to the X-ray energy. Therefore, X-ray mirrors can be used as cut-off filters of high-energy X-rays at an appropriate glancing angle.

A pseudo-toroidal mirror is usually used for the two-dimensional focusing of X-rays. Its radii of meridional ($R_m$) and sagittal ($R_s$) curvatures are

$$R_m = 2/\sin\theta_i \, (1/p + 1/q) \tag{12}$$

and

$$R_s = R_m \sin^2 \theta_i, \tag{13}$$

where $\theta_i$ is the glancing angle, $p$ is the distance between the mirror and the light source, and $q$ is the distance between the mirror and the focal point.

The use of these mirrors in the high-energy region of 20 - 40 keV will lead a large mirror length with a large radius of meridional curvature owing to the small glancing angles. Therefore, the focusing of high-energy X-rays is extremely difficult if a total reflection mirror is used as the focusing optical element.

Fig. 3 shows the critical angle and the radius of meridional curvature as a function of X-ray energy for a mirror coated with Pt ($p$ = 38 m, $q$ = 12.7 m). The critical angle decreases with increasing X-ray energy (see equation 11) whereas the radius of meridional curvature increases.

## 3.3. Bending monochromator

Bragg angles of perfect crystal monochromators such as silicon or germanium are about thirty times larger than the glancing angles necessary for total reflection mirrors. Therefore, the utilization of perfect crystals as focusing optical elements facilitates the design of bending devices used in association with the monochromators for high-energy X-rays.

There are two types of focusing monochromator commonly utilized at present; the triangular bending monochromator (Lemonnier, Fourme, Rousseaux & Kahn,

1978) and the so-called "sagittal focusing" monochromator (Sparks, Borie & Hastings, 1980; Matsushita, Ishikawa & Oyanagi, 1986).

In the next three subsections, these two monochromators and the two-dimensionally focusing monochromator are discussed.

### 3.3.1. Triangular bending monochromator

Fig. 4 shows schematic drawings of one-dimensional focusing monochromators in the meridional direction. In the four-point bending method (Fig. 4(a)), a rectangular crystal wafer is held by four columns and elastic deformation is realized by applying force to the two outer columns. In the triangular bending method (Fig. 4(b)), the base of a triangular wafer is fixed and force is exerted on the top of the wafer.

The meridional focusing monochromators can be classified into the Johann-type and the Johansson-type. In the former, the lattice plane is parallel to the crystal surface and the surface is bent cylindrically with $R_m$ radius of curvature. Here, $R_m/2$ is the radius of the Rowland circle (Fig. 5). X-rays from the light source (S) on the circle are reflected to the focus (F) which is also on the circle. The distance from the light source to the monochromator, $p$, is represented by

$$p = R_m \cos\left(\frac{\pi}{2} - \theta_B\right) = \frac{R_m \lambda}{2d}, \tag{14}$$

where $\theta_B$ is the Bragg angle, $\lambda$ is the X-ray wavelength, and $d$ is the spacing of the lattice plane.

The X-rays here do not pass completely through one focal point, and astigmatism appears.

In the later, the surface of the crystal wafer is polished cylindrically with the $R_m$ radius of curvature, and the crystal wafer is bent also with radius $R_m$. After bending, the polished surface fits the Rowland circle (Fig. 6). In this case, astigmatism disappears.

An asymmetric reflection geometry (see Appendix A) is commonly used in the meridional direction in many focusing monochromators. In the asymmetric Johann- and Johansson-type geometries, the crystal wafer is cut with an oblique angle $\alpha$ between the lattice plane and crystal surface (Fig. 7). This differs from the two methods mentioned above in that the incident and reflected beams can have different optical path lengths.

Under the Gunier condition, in which the X-ray source and the focal points are both on the Rowland circle (Fig. 7), the radius of meridional curvature $R_m$ is given by

$$R_m = \frac{p}{\sin(\theta_B + \alpha)} = \frac{q}{\sin(\theta_B - \alpha)} . \tag{15}$$

One-dimensional (meridional) focusing methods must be combined with another focusing element such as a total reflection mirror in order to realize two-dimensional focusing (Helliwell, *et al.* 1982).

### 3.3.2. Sagittal focusing monochromator

The sagittal focusing monochromator is, in general, used to obtain a pseudo-two-dimensional focal point (Sparks, Borie & Hastings, 1980). The geometry of this monochromator is shown in Fig. 8, in which anticlastic bending of the second crystal is shown. The sagittal bending of the rectangular thin wafers results in an additional curvature at right angles. This additional curvature $R_{\bar{m}}$ is related to the radius of sagittal curvature $R_s$ by

$$R_{\bar{m}} = R_s / \sigma , \tag{16}$$

where $\sigma$ is Poisson's ratio.

In order to eliminate anticlastic bending, a structure with ribs behind the second crystal is proposed, as shown in Fig. 9 (Sparks, Ice, Wong & Batterman, 1982).

High-energy X-ray reflection is sensitive to crystal distortion because the Darwin width $W_h$ decreases depending on wavelength $\lambda$ (inversely proportional to the energy value) as

$$W_h = (e^2 / mc^2)(\lambda^2 / v\pi \sin\theta_B) F_h . \tag{17}$$

The ribs behind the crystal cause distortions between the rib and non-rib positions. To remove these distortions one should use the rib side as the reflective face, as shown in Fig. 10 (Mills, Henderson & Batterman, 1986).

The applicability of this method is limited by the fact that the focus size may be larger than the rib size. Furthermore, its application to X-rays from an undulator is considered to be difficult since the size of the X-ray beam is too small to be converged with the sagittal focusing geometry.

### 3.3.3. Two-dimensionally focusing monochromator

In the previous two subsections, the two-dimensional focusing of high-energy X-rays from the undulator was shown to be difficult. However, there is a possibility that anticlastic bending caused by the sagittal bending can be canceled out by meridional bending.

Fig. 11 shows a two-dimensional focusing monochromator simultaneously bent in the two directions. In this case, the focal lengths have to be adjusted in both the meridional and sagittal directions. The radius of sagittal curvature ($R_s$) should satisfy the following relationship:

$$R_s = R_m\left(\sin^2\theta_B - \sin^2\alpha\right). \tag{18}$$

There are various types of two-dimensional focusing monochromator fabricated using lithium fluoride (Sakabe, 1983), germanium (Wittry & Golijanin, 1988), quartz (Berreman, Stamatoff & Kennedy, 1977; Förster, Gäbel & Uschmann, 1992), and silicon crystals (Kawata, Sato, Higashi & Yamaoka, 1994). None of these, however, are tunable in the X-ray energy range. Since tunability is an indispensable function of monochromators used in protein crystallography, these monochromators cannot, unfortunately, accommodate the present purpose.

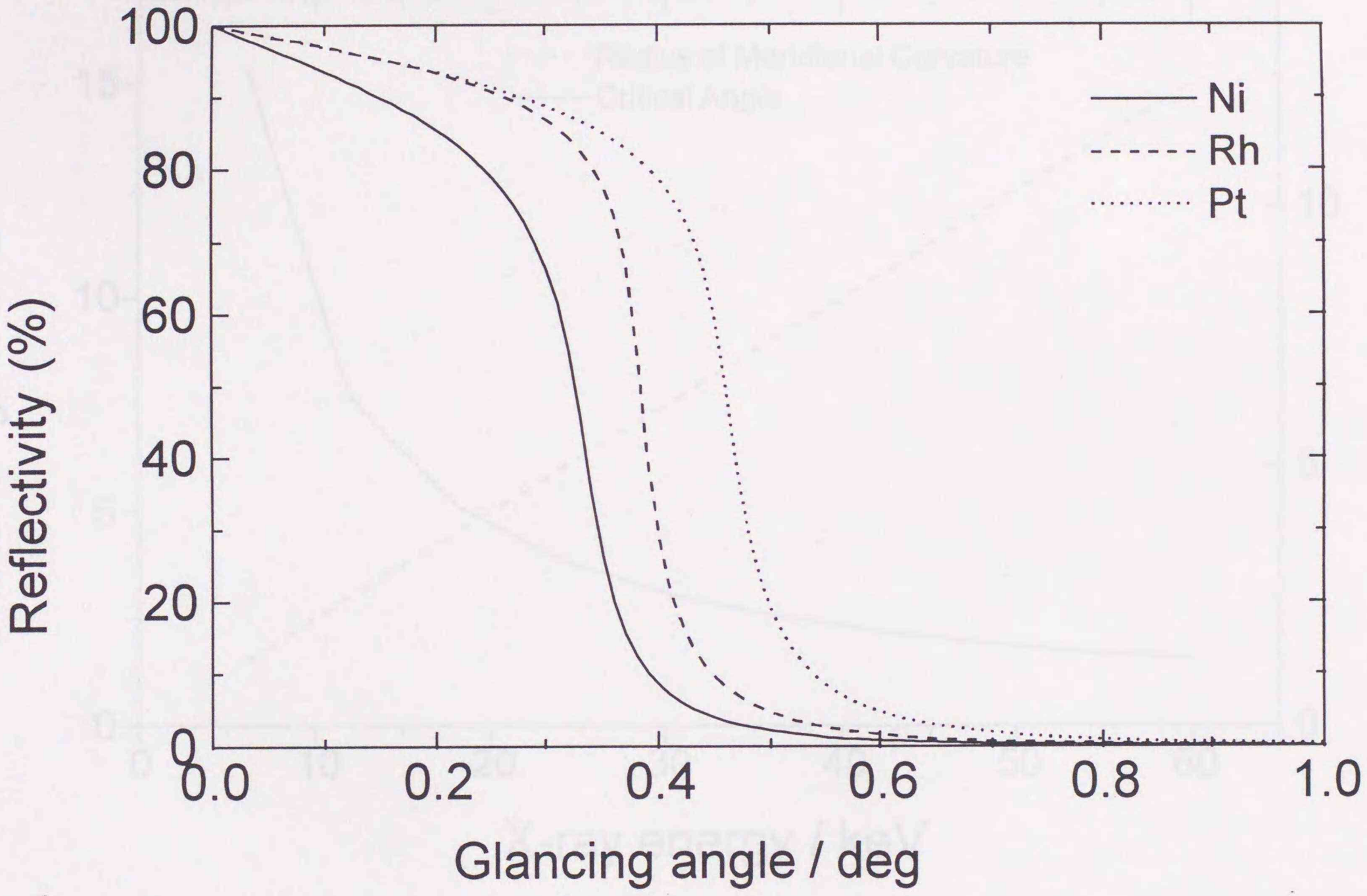


Fig. 2 : The glancing angle dependence of the reflectivity of X-ray mirrors coated with Ni, Rh or Pt. The X-ray energy is 10 keV.

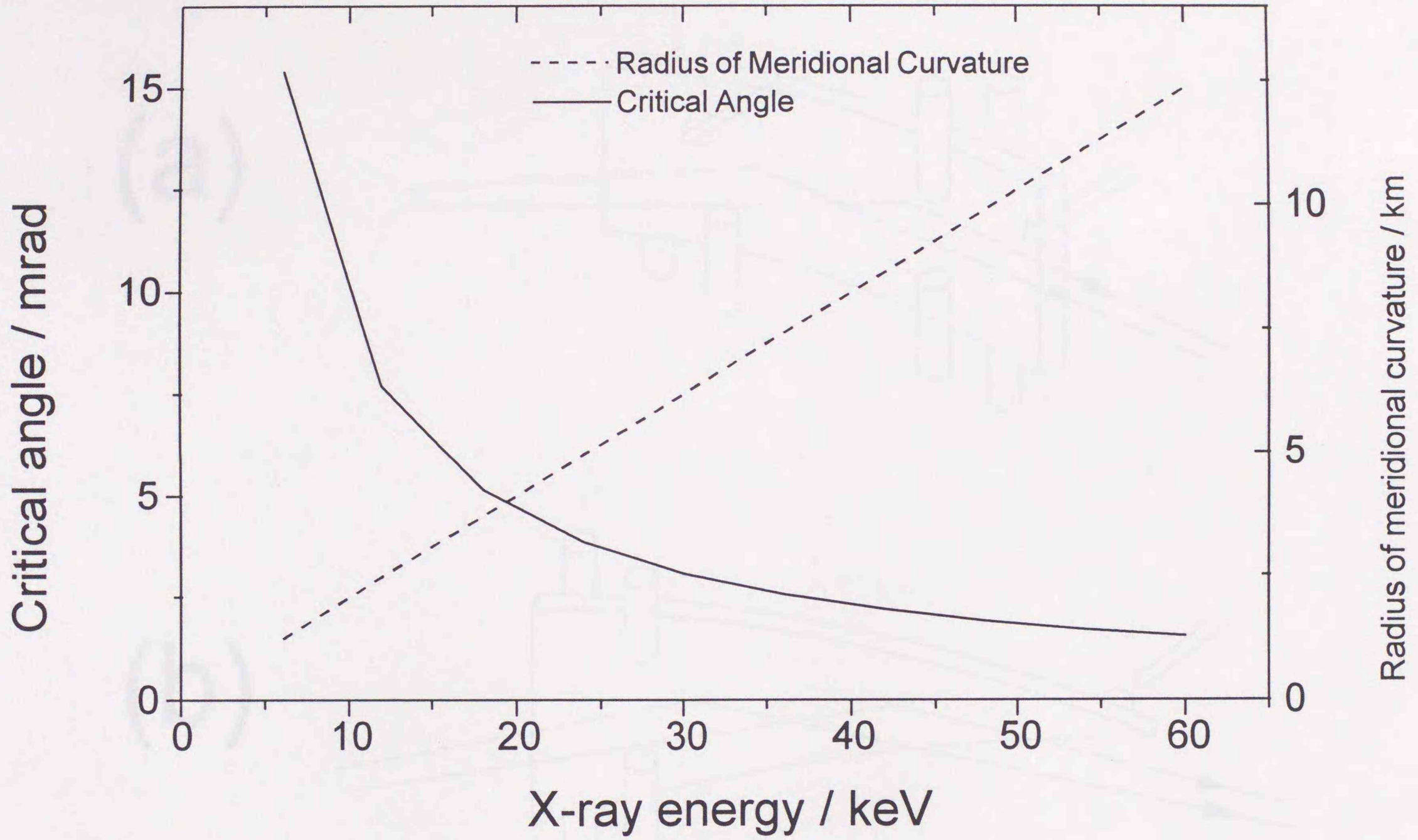


Fig. 3 : The energy dependence of the critical angle and radius of meridional curvature for a focusing X-ray mirror coated with Pt.

(a)

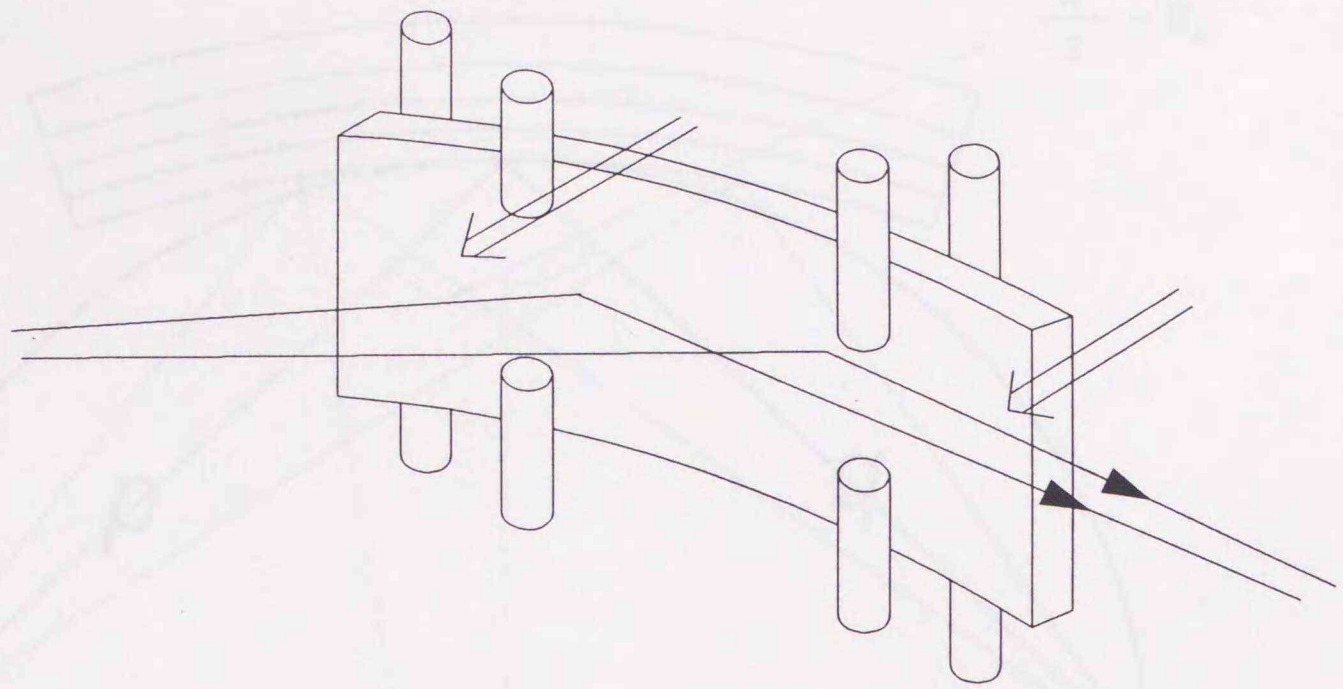

(b)

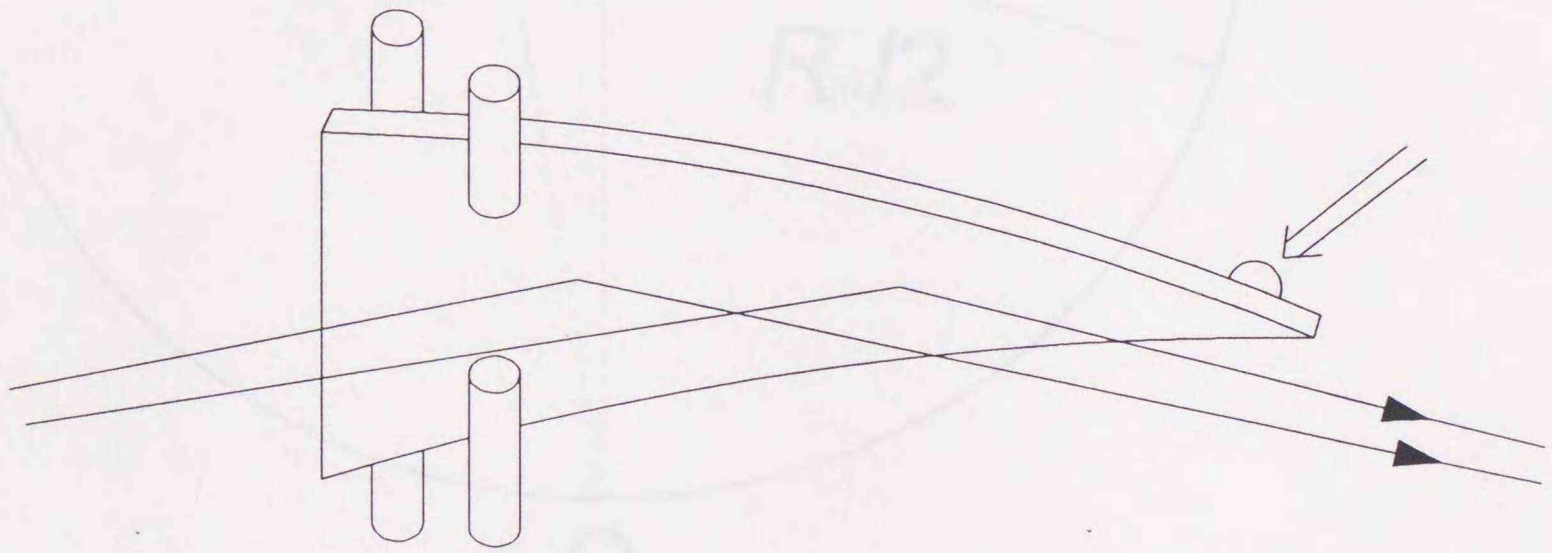

Fig. 4 : Two methods of one-dimensional bending.

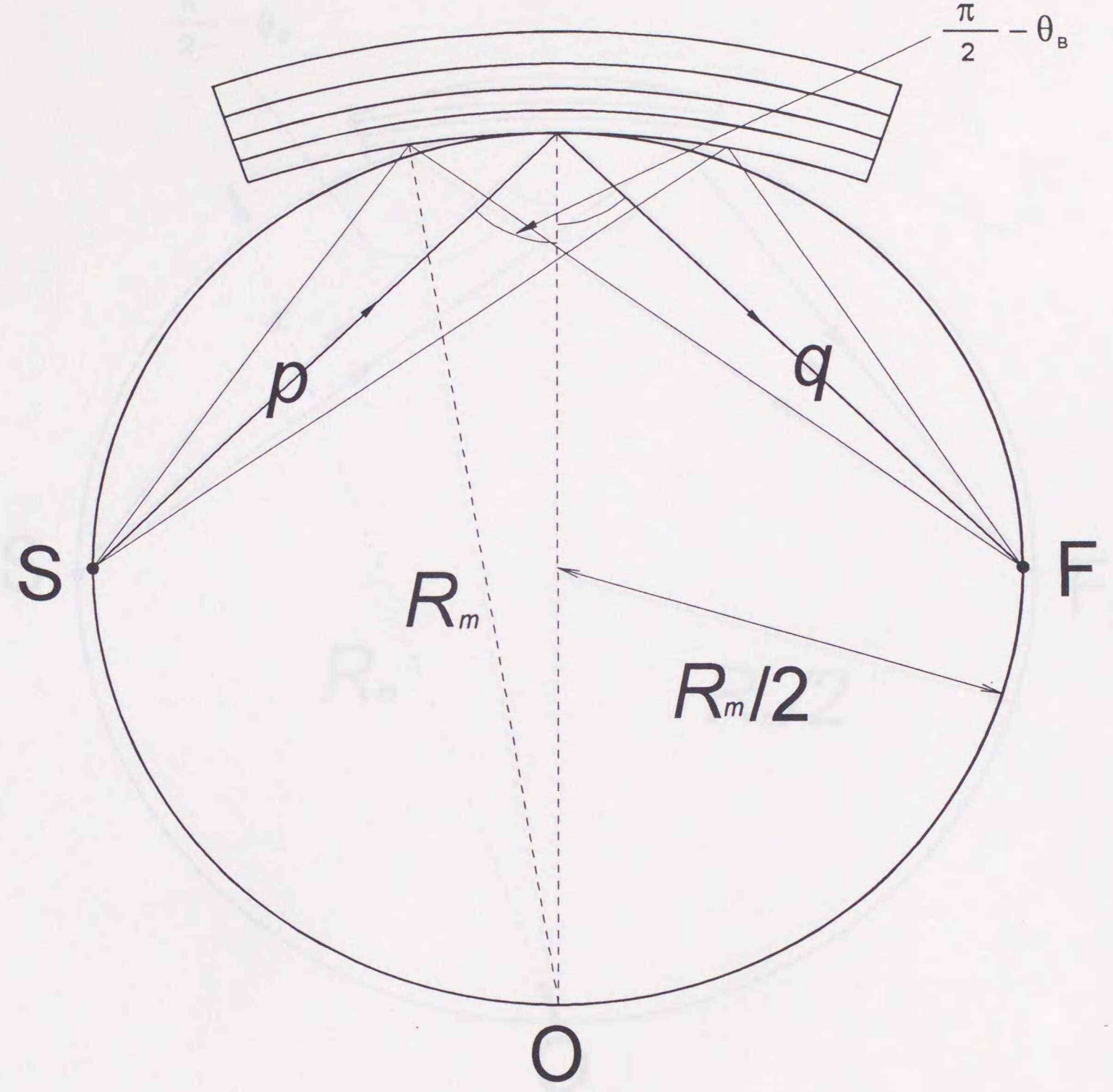


Fig. 5: Johann-type crystal monochromator.

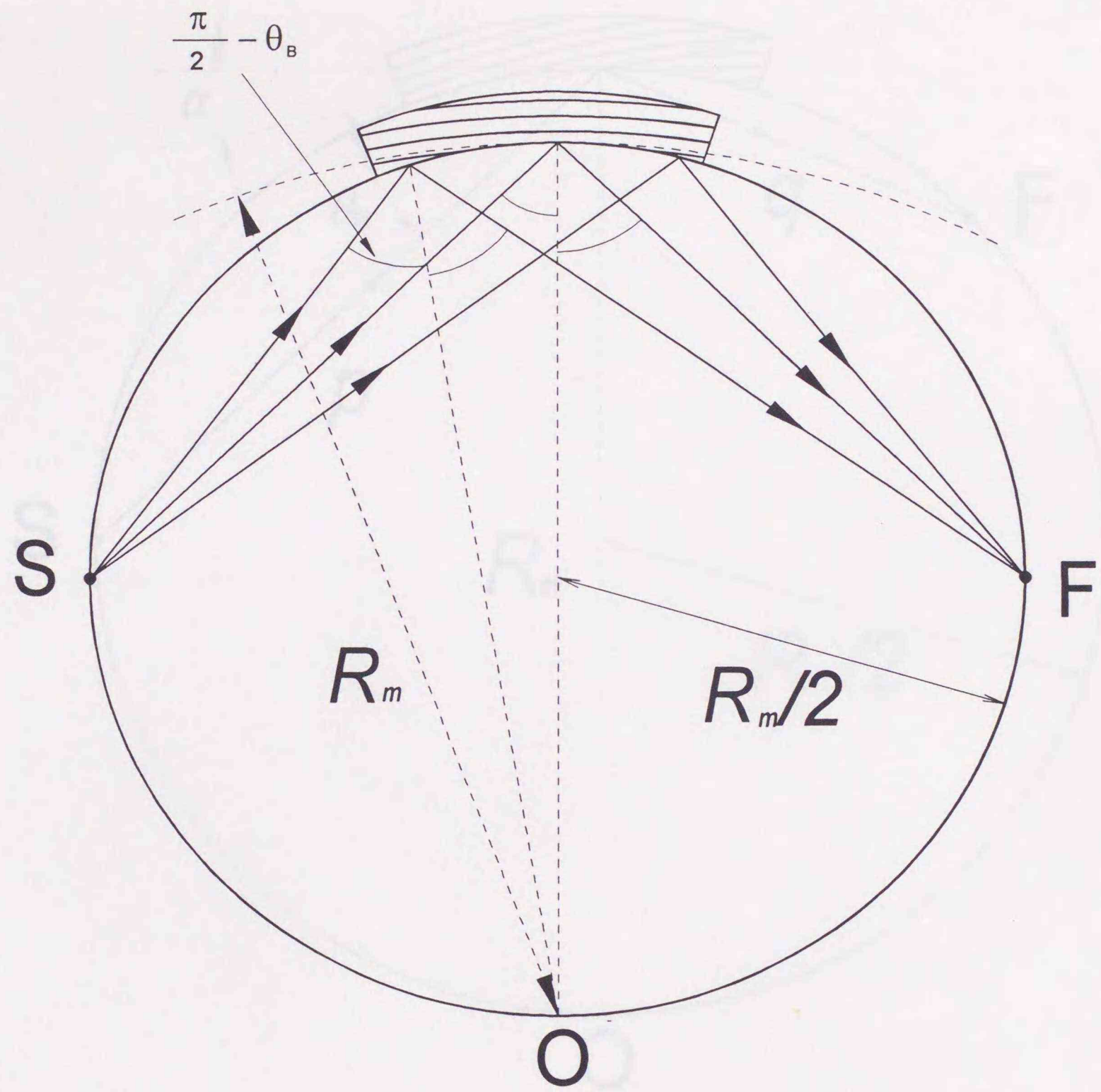


Fig. 6: Johansson-type (symmetric).

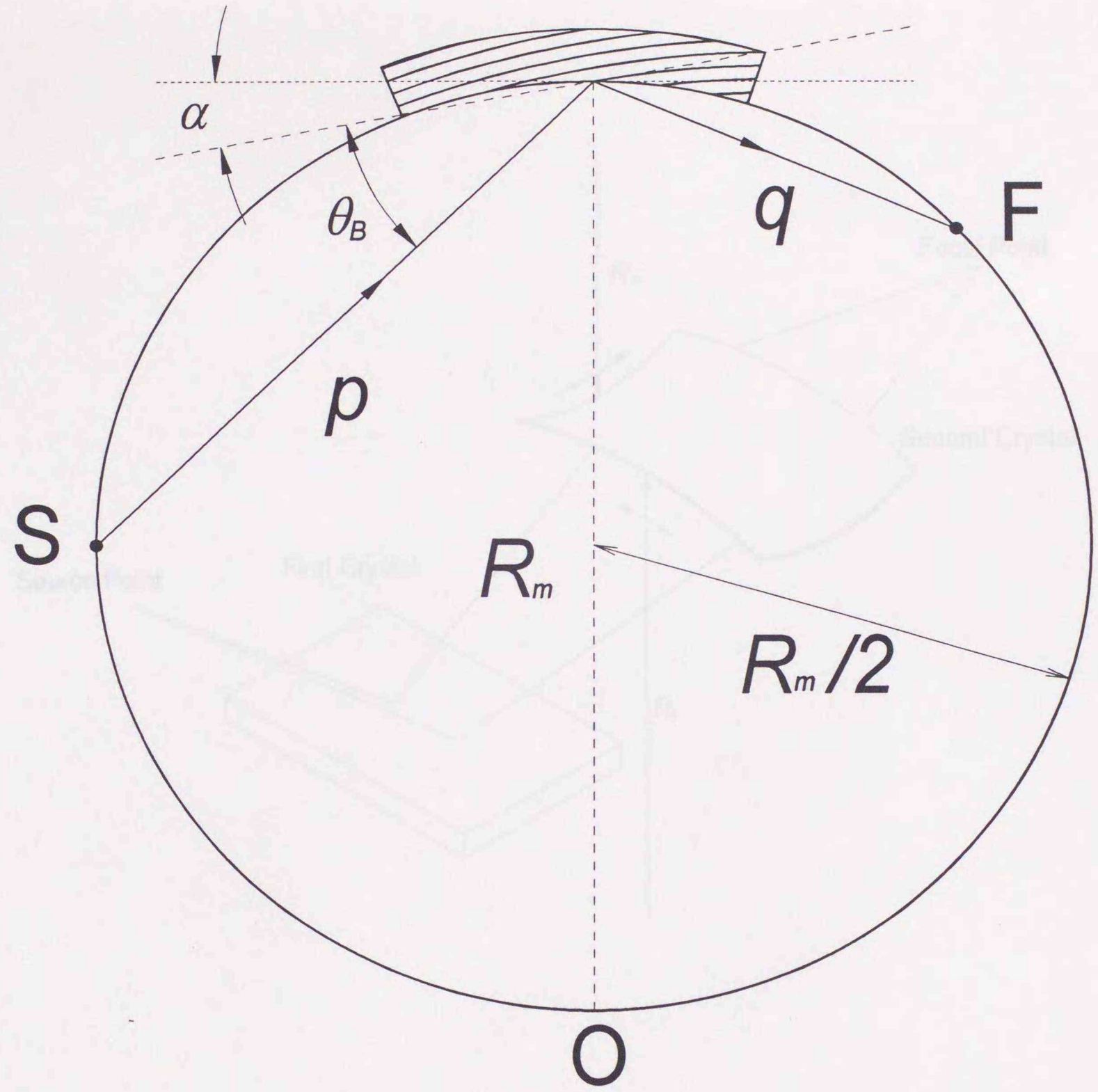


Fig. 7: Johansson-type (asymmetric).

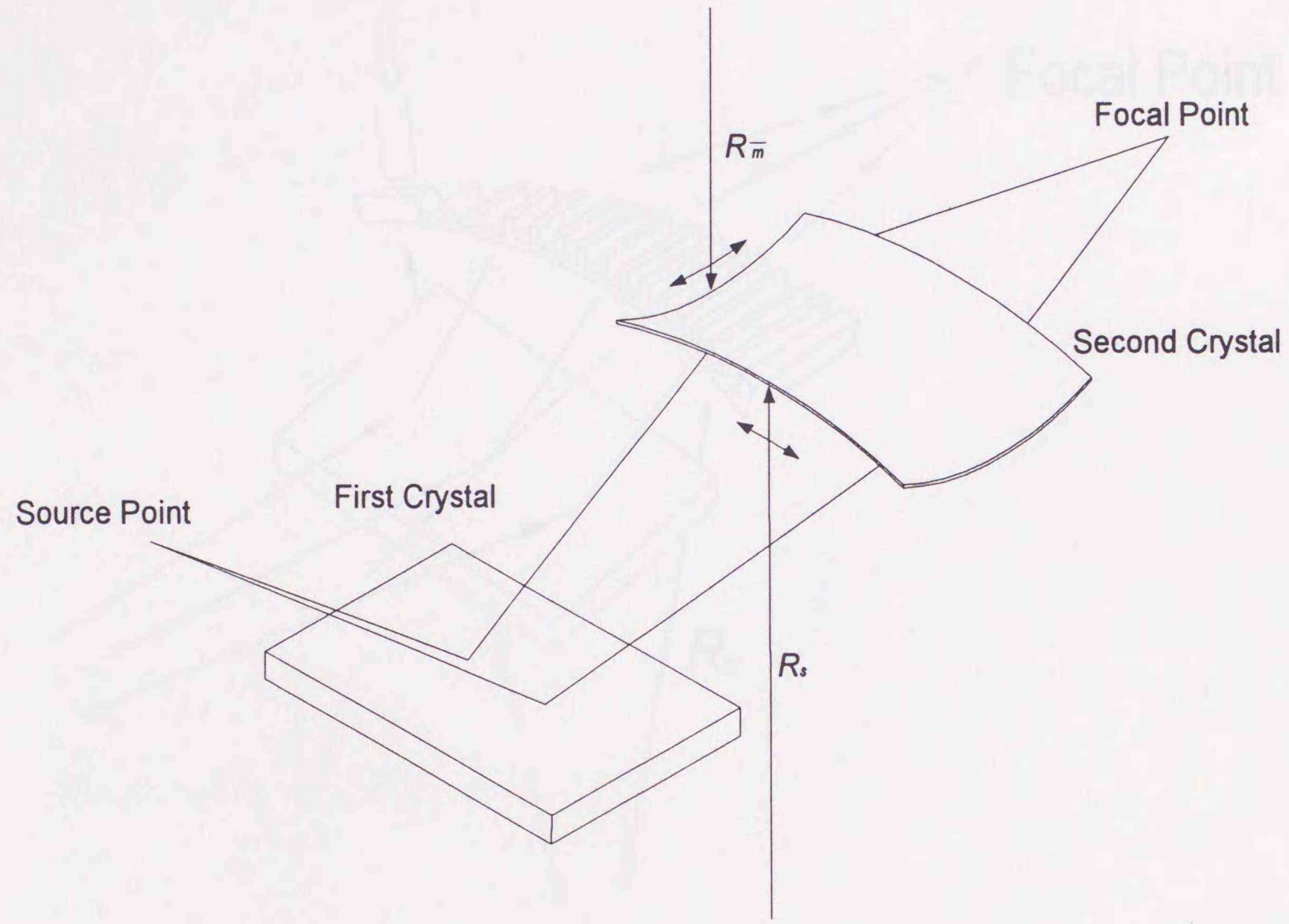


Fig. 8: Arrangement of sagittal focusing monochromator.

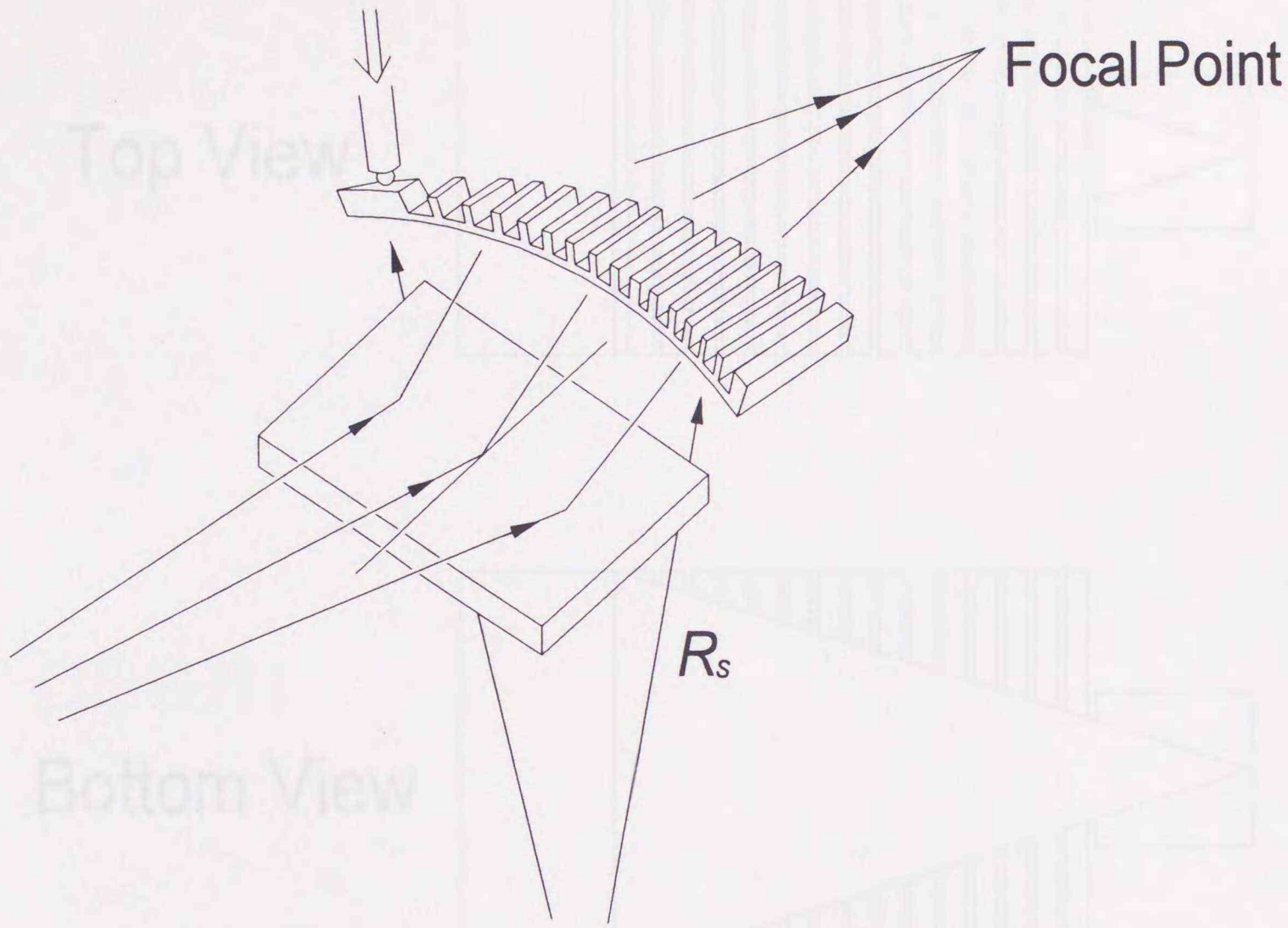


Fig. 9 : Schematic drawing of sagittal focusing monochromator with ribs.

Top View

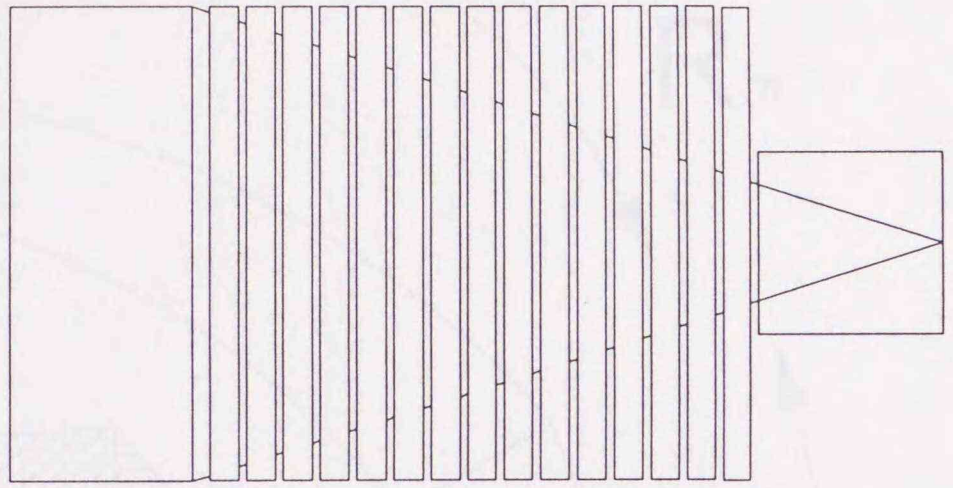

Bottom View

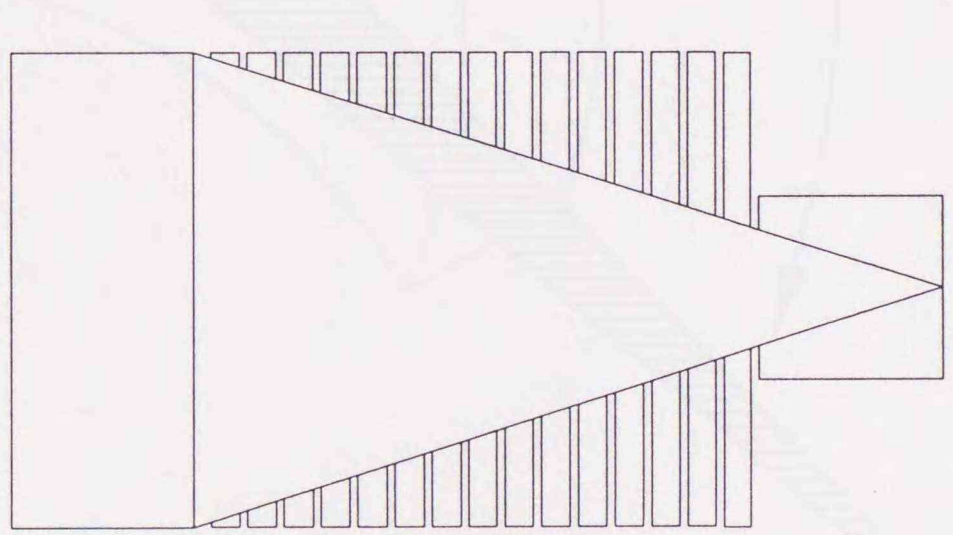

Fig. 10: Example of use of rib side.

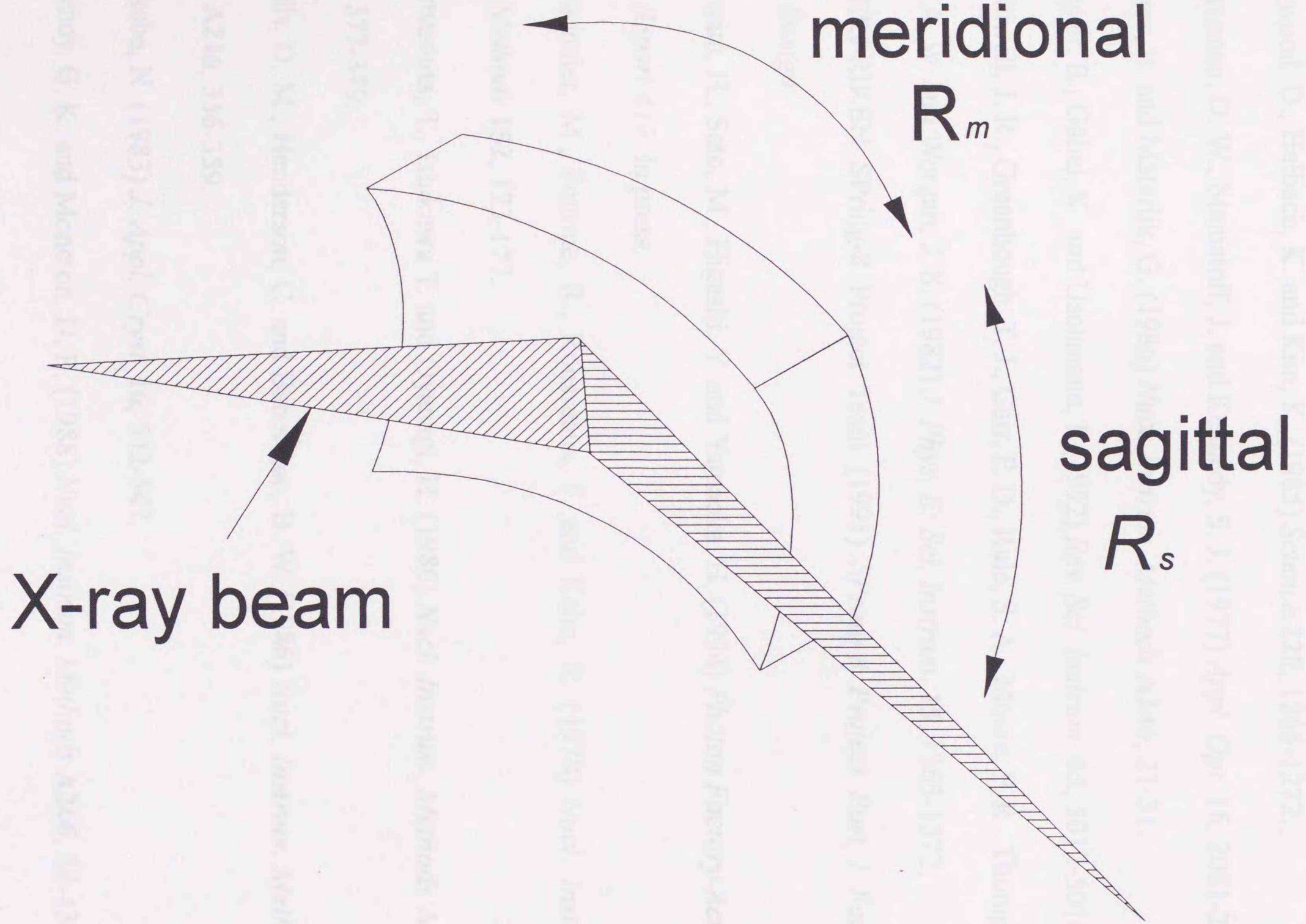


Fig. 11: Double Focusing.

# References


Attwood, D., Halbach, K. and Kim, K. (1985) *Science* **228**, 1265-1272.

Berreman, D. W., Stamatoff, J. and Kennedy, S. J. (1977) *Appl. Opt.* **16**, 2081-2085.

Buras, B. and Materlik, G. (1986) *Nucl. Instrum. Methods* **A246**, 21-31.

Förster, E., Gäbel, K. and Uschmann, I. (1992) *Rev. Sci. Instrum.* **63**, 5012-5016.

Helliwell, J. R., Greenhough, T. J., Carr, P. D., Rule, S. A., Moore, P. R., Thompson, A. W. and Worgan, J. S. (1982) *J. Phys. E: Sci. Instrum.* **15**, 1363-1372.

JAERI-RIKEN SPring-8 Project Team (1991) *SPring-8 Project Part I Facility Design.*

Kawata, H., Sato, M., Higashi, Y. and Yamaoka, H. (1994) *Photon Factory Activity Report #12.* In press.

Lemonnier, M., Fourme, R., Rousseaux, F. and Kahn, R. (1978) *Nucl. Instrum. Methods* **152**, 173-177.

Matsushita, T., Ishikawa T. and Oyanagi, H. (1986) *Nucl. Instrum. Methods* **A246**, 377-379.

Mills, D. M., Henderson, C. and Batterman, B. W. (1986) *Nucl. Instrum. Methods.* **A246**, 356-359.

Sakabe, N. (1983) *J. Appl. Cryst.* **16**, 542-547.

Shenoy, G. K. and Moncton, D. E. (1988) *Nucl. Instrum. Methods* **A266**, 38-43.

Sparks, C. J., Borie, B. S. and Hastings, J. B. (1980) *Nucl. Instrum. Methods* **172**, 237-242.

Sparks, C. J., Ice, G. E., Wong, J. and Batterman, B. W. (1982) *Nucl. Instrum. Methods* **194**, 73-78.

Wittry, D. B. and Golijanin, D. M. (1988) *Appl. Phys. Lett.* **52**, 1381-1382.

Yamamoto, S., Shioya, T., Hara, H., Kitamura, H., Zhang, X., Mochizuki, T., Sugiyama, H. and Ando, M. (1992) *Rev. Sci. Instrum.* **63**, 400-403.

# 4. Design and Simulation

In the following sections, the designs of two types of two-dimensional benders and their performances are discussed.

## 4.1. Design of two-dimensionally tunable focusing monochromator

Table 2 (Kawano & Kamiya, 1996) shows the design parameters for the present two-dimensional focusing monochromator (Johann type). These values were determined so as to adequately examine the focusing ability of the monochromator at beamline 15B of the Photon Factory (PF) of the National Laboratory for High-Energy Physics, where the distance between its source point and the experimental station was as long as that expected at the SPring-8 undulator beamline. Since the oblique-cut angle $\alpha$ depends upon individual beamlines, the final values of the parameters for the SPring-8 beamline will be subject to careful reconsideration based on the actual values of $p$ and $q$, and the tunable range of X-ray energy, among others.

Table 2 : Design parameters

| | |
|---|---|
| distance from source to monochromator ($p$) | 37.0 m |
| distance from monochromator to focus ($q$) | 4.47 m |
| X-ray energy | 37.7 keV |
| Bragg angle ($\theta$) of Si (111) | 3.008 deg |
| oblique-cut angle ($\alpha$)* | -2.36 deg |
| asymmetry factor ($b$)* | 8.27 |
| radius of meridional curvature ($R_m$)* | 396 m |
| radius of sagittal curvature ($R_s$)* | 0.42 m |

*) definitions are given in the text.

## 4.2. Prototype 1 bender

Fig. 12 shows the outline of the prototype 1 bender (Kamiya & Iwasaki, 1992). It uses the four-point bending mechanism independently in the meridional (horizontal) and sagittal (vertical) directions. Two I-beams (B) are used for meridional bending and a board spring (C) is used for sagittal bending. Blocks in the sagittal bender are held with screws (D) and the curvature in the sagittal direction is adjusted independently. This bender operates smoothly when the radius of sagittal curvature is large. However, when the sagittal radius of curvature becomes small, local distortion arises in the silicon wafer and it is easily destroyed because tuning of the blocks in the sagittal bender becomes difficult.

## 4.3. Prototype 2 bender

The radii of meridional and sagittal curvatures of the silicon wafer were changed independently by rotating four screws (two pairs each of $T_m$ and $T_s$) in a special bender, as shown in Fig. 13 (Kawano & Kamiya, 1996). The bender had eight holders, fixing the horizontal and vertical positions of each leg of the copper table. The horizontal ($A_h$-$D_h$) and vertical ($A_v$-$D_v$) holders were placed on corresponding cross-roller guides (eliminated in Fig. 13 for clarity), and roller bearings perpendicular to the cross-roller guides were included in the holders in order to reduce possible frictional forces produced during expansion of the spaces between the legs of the table. The expansion of the spaces would result in alterations in the radii of curvature.

## 4.4. Improvement of bonding method of silicon wafer

When the entire surface of a silicon wafer is bonded to the copper block (B1 of Fig. 14), considerable undulation is generated due to differences in bonding strengths at different positions. In order to remove the undulation, two kinds of spacers (B2 and B3, made of phosphorus bronze of 0.5 mm thickness) were inserted in the space between the copper block and the silicon wafer (Kamiya, *et al*. 1993). Although the undulation disappeared when the monochromator was bent in both directions, optical warping occurred (see images of two parallel straight lines on the silicon wafer). The width between the two lines is proportional to the radius of the monochromator curvature. That is, the introduction of spacers leads to a positional dependence on the radius of sagittal curvature. However, this problem is not a serious one because the undulator beam size of the SPring-8 is very small, about 1 mm. This means that a two-dimensional monochromator with an effective area of 20 mm in the meridional direction is necessary.

For the present two-dimensional focusing monochromator, a silicon (111) wafer of 40 × 100 mm area (much wider than the effective area required) and 0.5 mm thickness, which was fabricated by Sharan Instruments Company, Ltd, was employed. The silicon wafer is adhered onto a tablelike copper block with epoxy glue, as shown in Fig. 15. A hillock of 0.5 mm height with a 25 × 70 mm hollow in the center is made on the table surface instead of the spacer B2.

## 4.5. Simulation of two-dimensionally curved shape

As already mentioned, anticlastic bending in the meridional direction of the monochromator wafer can be established by bending the wafer with a small radius of sagittal curvature when the wafer has mechanically free edges (Sparks, Ice, Wong, & Batterman, 1982). In the present two-dimensional focusing monochromator, however, a resultant change in shape of the monochromator wafer was not evident at all, since the boundaries of the wafer were adhered on the tablelike copper block.

In order to evaluate the deviation of the actual surface from the toroidally curved one, the shape of the monochromator surface was simulated by the finite-element method, taking the structural effect of the tablelike copper block into consideration. A one-fourth model of the monochromator (Fig. 16) was simulated using the software program ANSYS of Swanson Analysis Systems, Inc. Acceleration due to gravity was not considered in this calculation. Bending of the monochromator was achieved by assuming that the origin point is fixed and by applying on external force from the inside to the foot of the tablelike copper block.

First, the simulation was carried out by applying force only in the sagittal direction. The radius of curvature became 1.5 m and anticlastic bending was generated. Afterwards, anticlastic bending decreased when force was applied in the meridional direction (Fig. 17 (a)-(f)). When the ratio of forces applied in the meridional and sagittal directions was 8 : 1, anticlastic bending in the meridional direction almost disappeared (Fig. 17 (f)).

Fig. 18 (a) shows a simulated trace along the centerline in the meridional direction in Fig. 17 (f). Although the overall trace can be regarded approximately as

a circle, the detailed structure of the trace near the center must be carefully examined, since it is the central area (±10 mm) that will be irradiated by the small X-rays from the undulator. Fig. 18 (b) shows the central region of Fig. 18 (a) with a magnification factor of three. This radius of curvature near the center is larger than those of adjacent areas. This feature can also be regarded as a pair of bending components with a smaller radius of curvature than the ideal value, arranged side by side with a small separation.

The deviation of the calculated trace from an ideal circle is very small, i.e., within ±10 mm. Using the least squares method, the root-mean-square deviation (RMSD) from an ideal circle of 141 m radius (broken line) was calculated to be only 0.051 μm for the present case. On the other hand, as regards the simulated trace in the sagittal direction, a feature such as that observed in the meridional direction was not found (data not shown), and the averaged radius of curvature deduced was 1.14 m with an RMSD of 0.041 μm in the central region of ±1 mm.

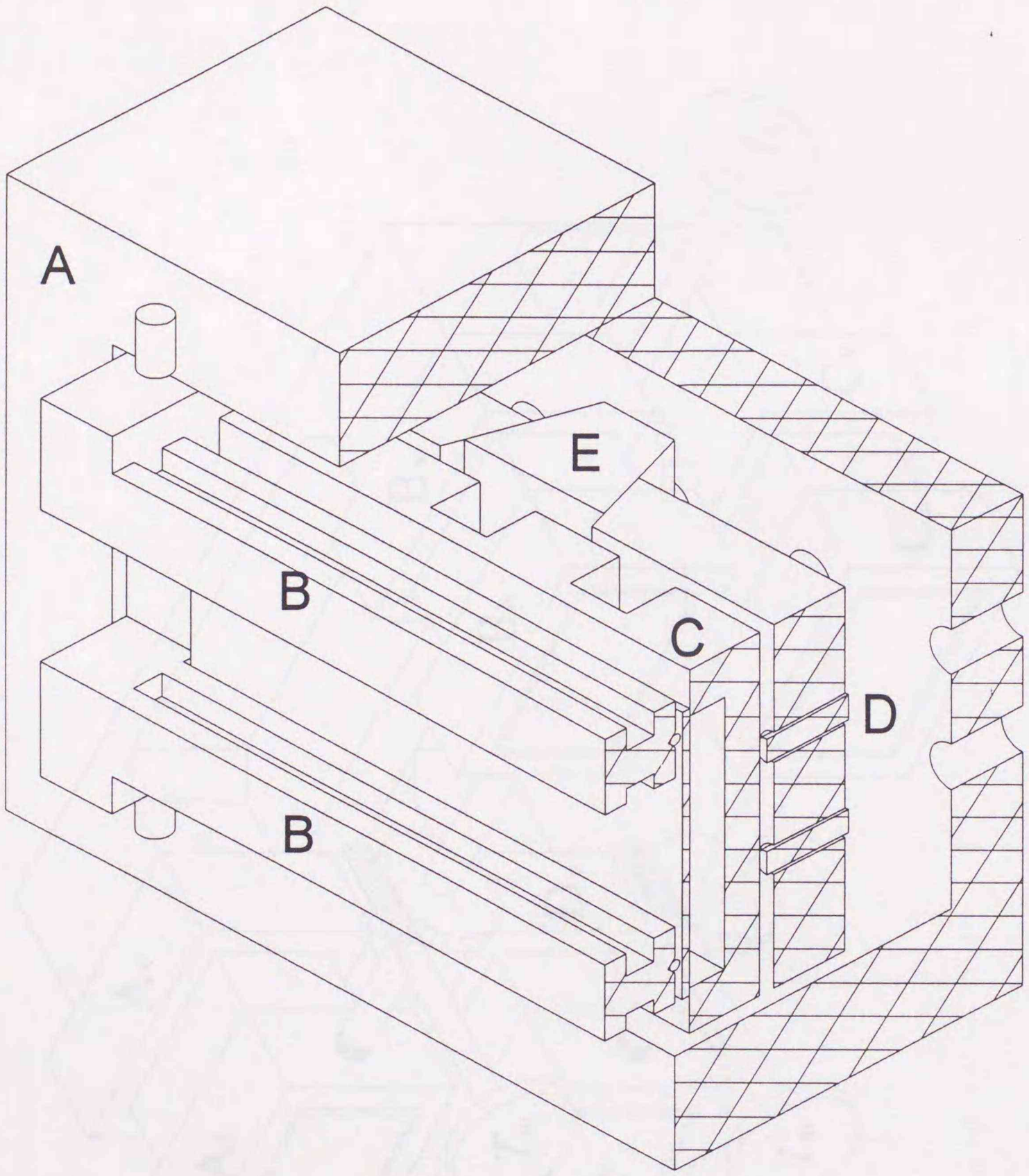


Fig. 12: Bending mechanism of a two-dimensionally tunable focusing monochromator (Prototype 1). Silicon wafer (40 mm x 80 mm x 0.5 mm) is inserted between the meridional bender (*B*) which consists of two I-beams and the sagittal bender (*C*) which consists of a board spring. These are stored in the outside frame (*A*). Each block of the sagittal bender is pushed with screws (*D*). After bending in the sagittal direction, meridional bending is realized by drawing out a piece (*E*) at the center of the meridional bender from the back of the outside frame using a screw (not shown).

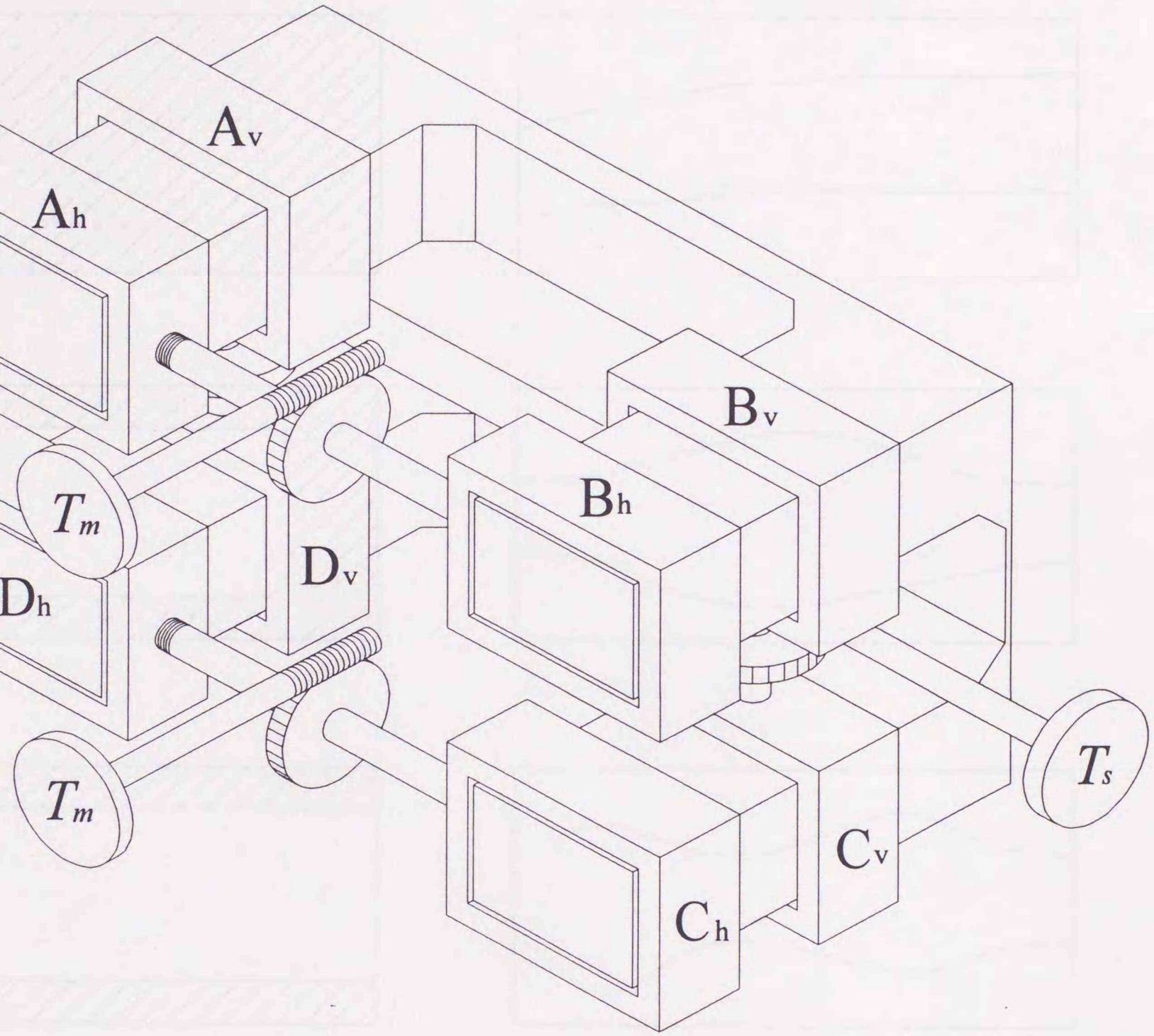


Fig. 13 : Bending mechanism of two-dimensionally tunable focusing monochromator (Prototype 2).

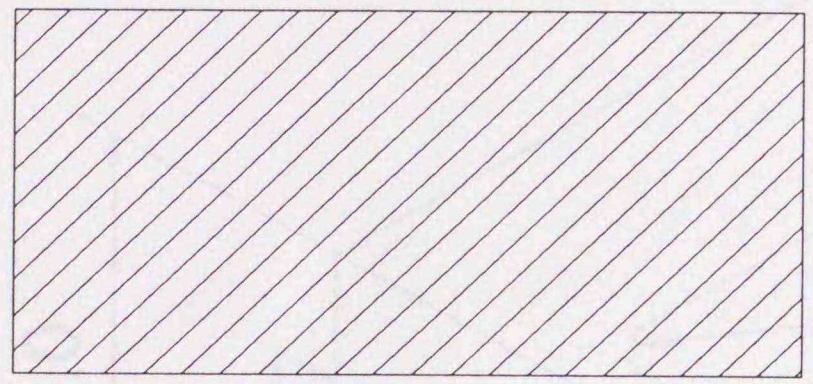

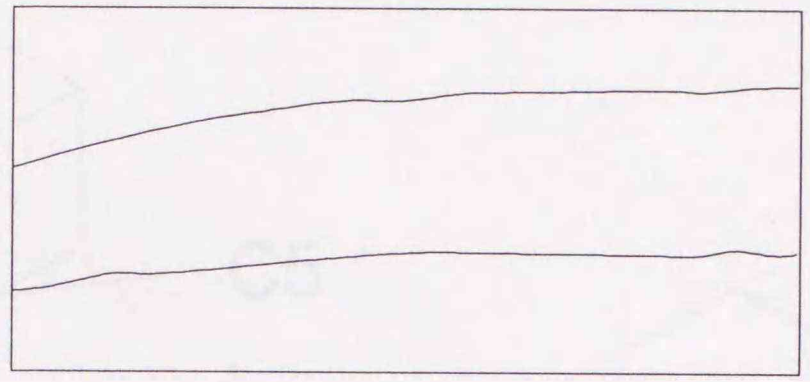

B1

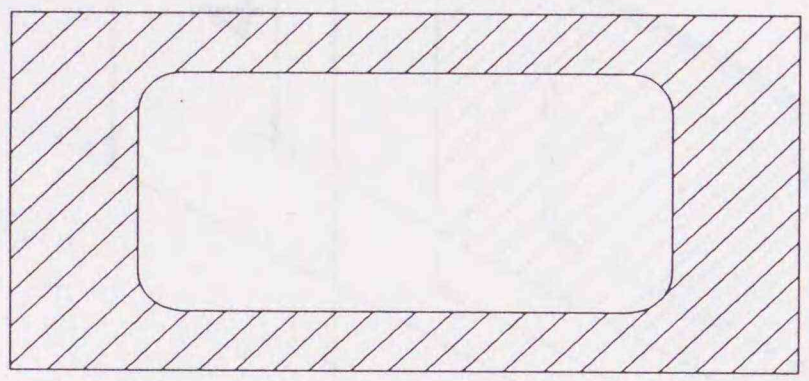

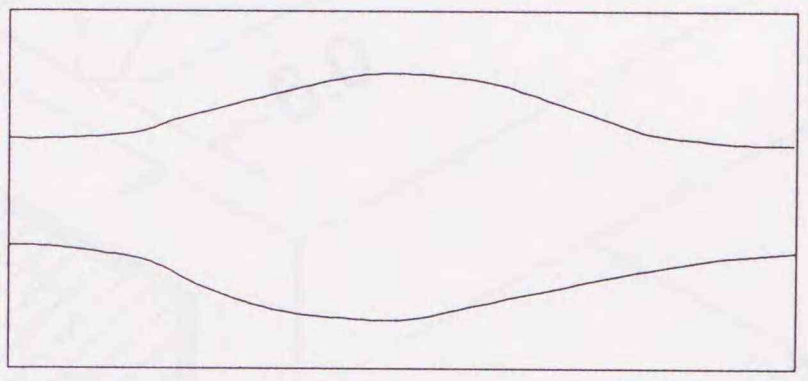

B2

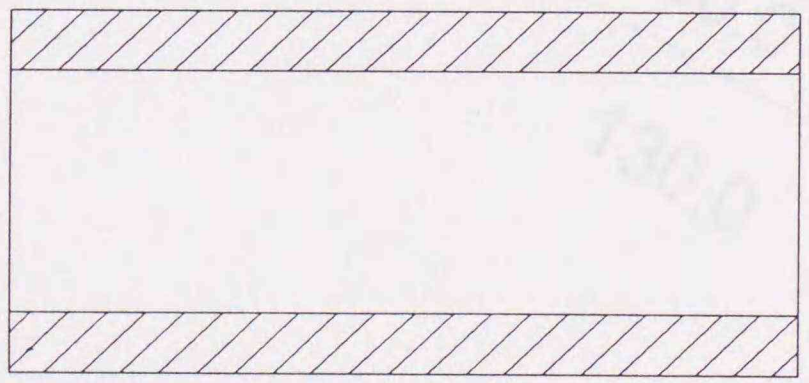

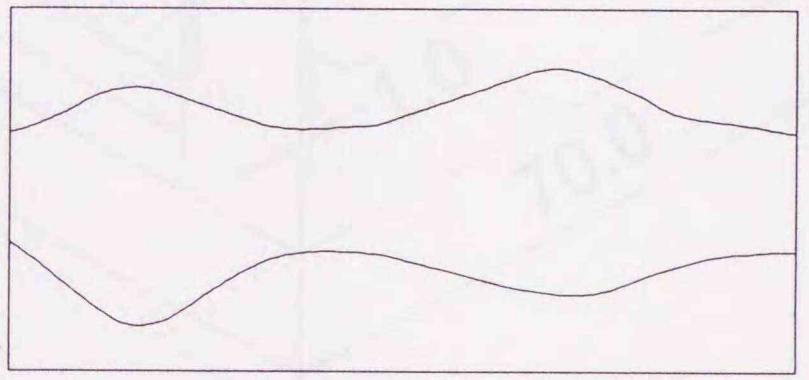

B3

Fig. 14 : Bonding method and optical warp of silicon wafer.

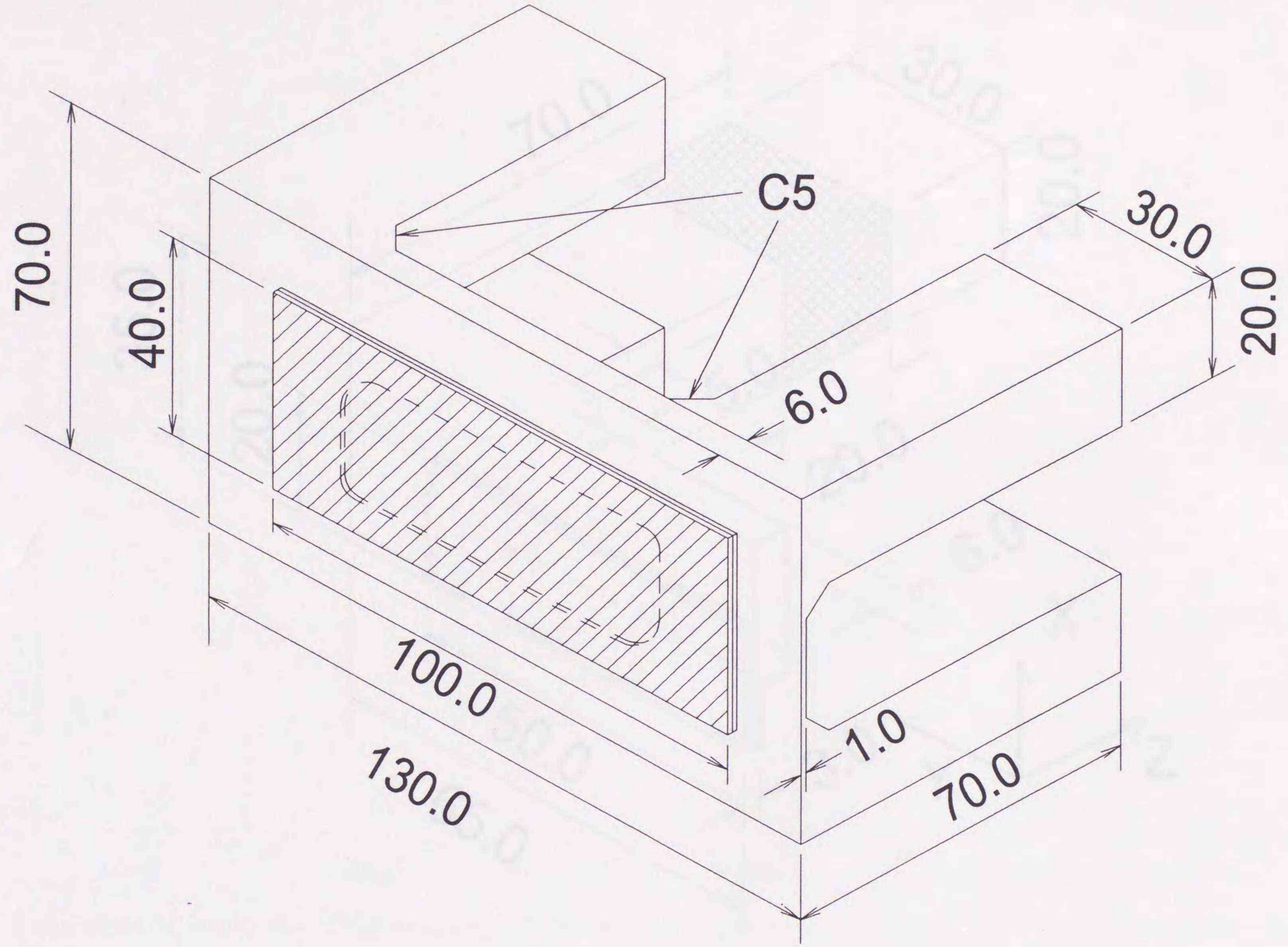


Fig. 15 : Schematic drawing of two-dimensionally tunable focusing monochromator. Si wafer (hatched) glued on a tablelike copper block. Dimensions are in millimeters. C5: 5 x 5 mm corner.

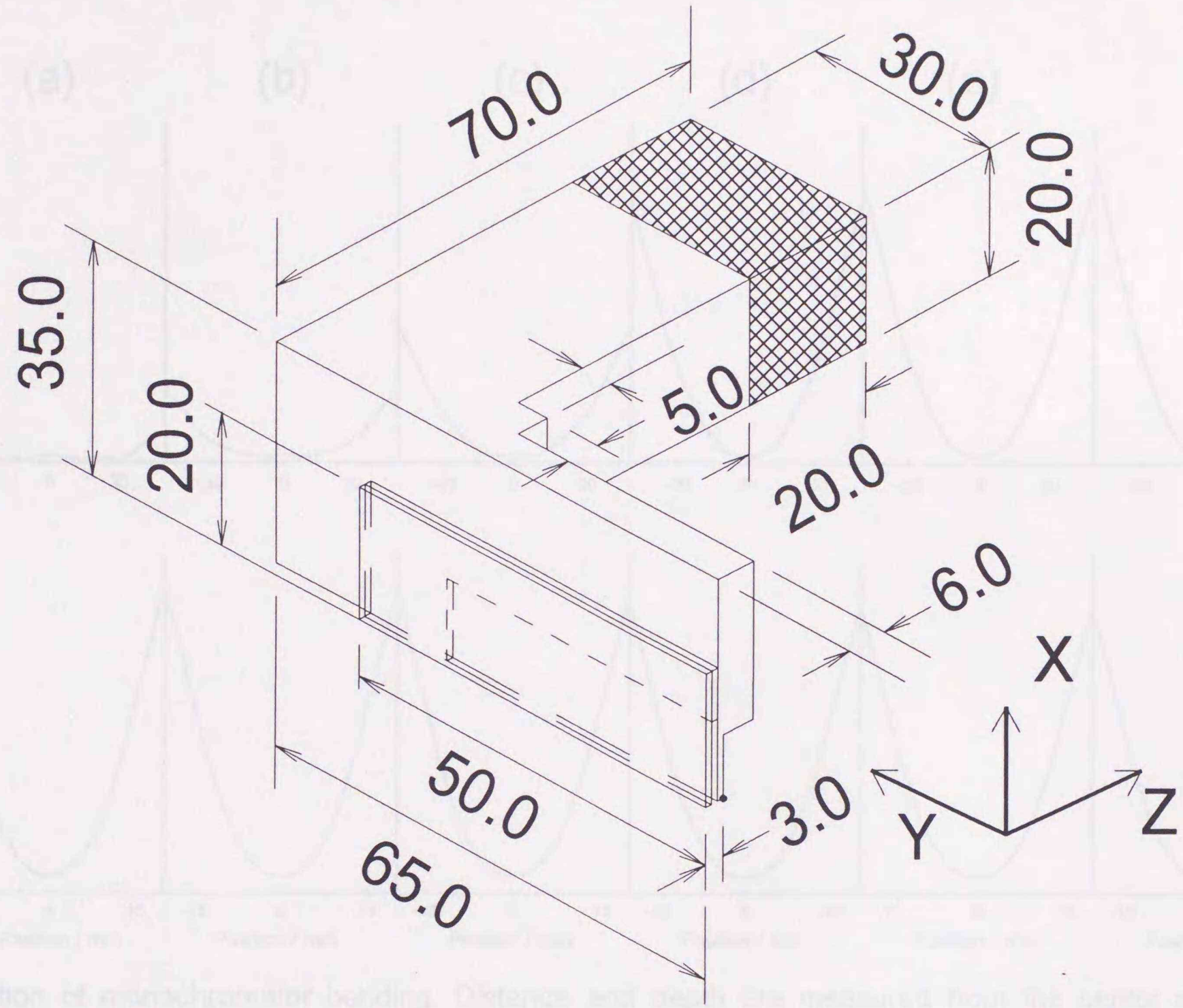


Fig. 16 : Model for *ANSYS* calculation. A 1/4 model of the tablelike copper block including the silicon wafer was used for simulation. The origin of the model system is the center of copper table. The cross-hatched part is that where the force is applied. Si wafer is glued on a tablelike copper block. Dimensions are in millimeters.

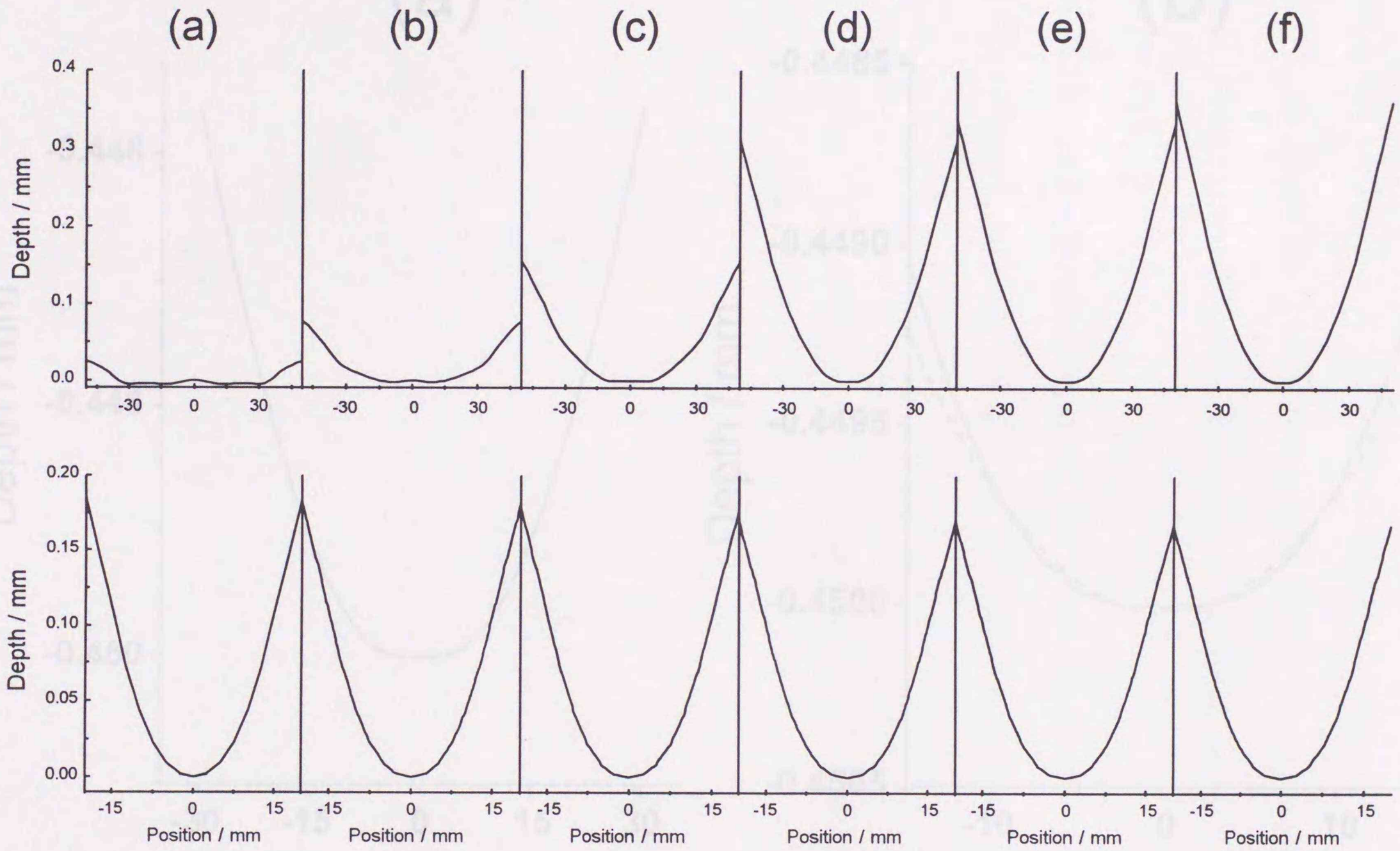


Fig. 17 : Simulation of monochromator bending. Distance and depth are measured from the center and edge of the monochromator wafer, respectively. Upper figures are for the meridional direction. Lower figures are for the sagittal direction. In (*a*), the ratio of applied forces in sagittal and meridional directions is 2 to 3. (*b*); 2 to 5. (*c*); 1 to 4. (*d*); 1 to 7. (*e*); 2 to 15. (*f*); 1 to 8.

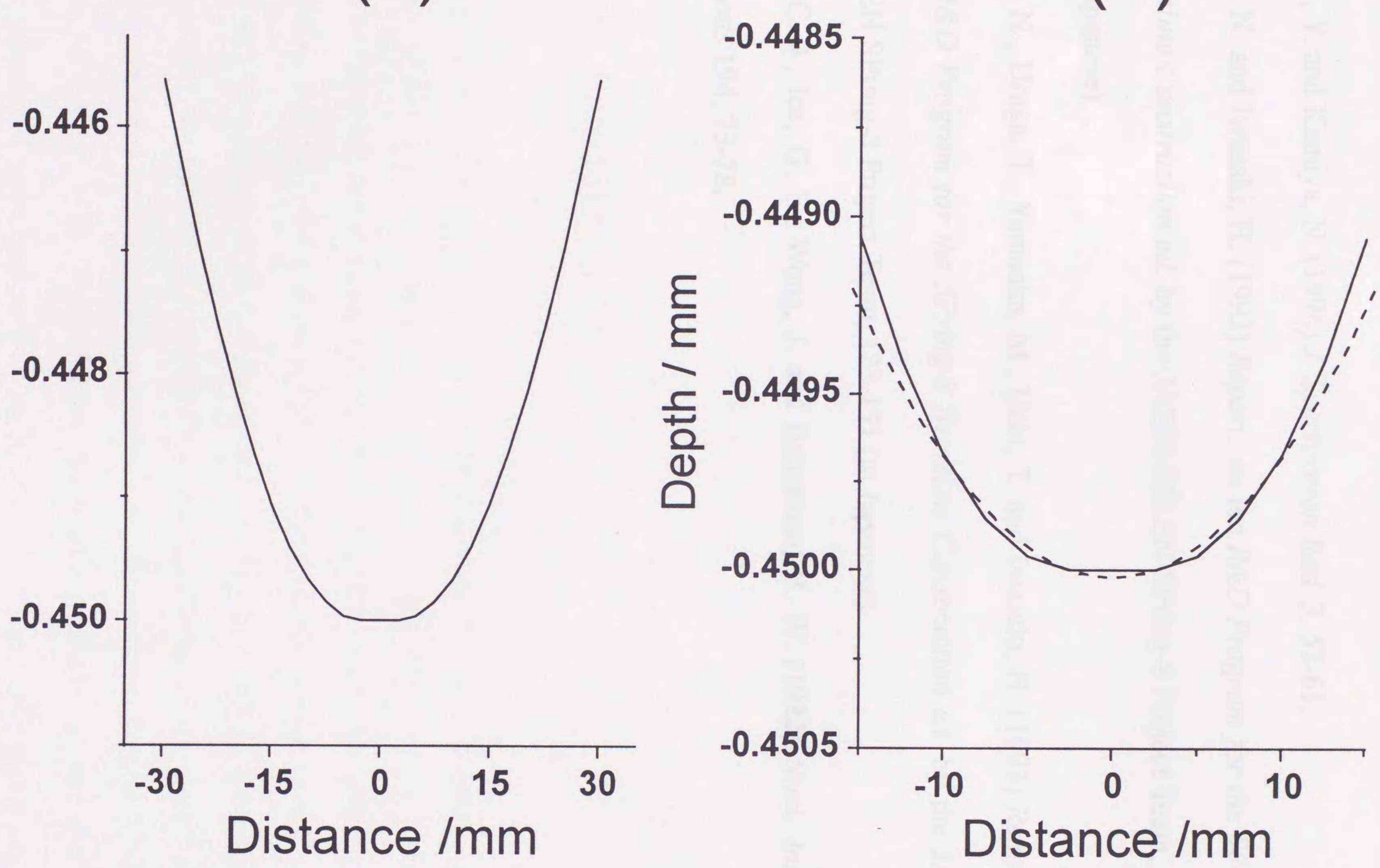


Fig. 18 : Simulation in meridional direction of (*f*) in Fig. 17. (*a*) ±30 mm area around the center, and (*b*) threefold magnification of the ±10 mm area. Continuous line: simulated trace. Broken line: least squares fit of an ideal circle. Distance and depth are measured from the center and edge of the monochromator wafer, respectively.

# References


Kawano, Y. and Kamiya, N. (1996) *J. Synchrotron Rad.* **3**, 53-61.

Kamiya, N. and Iwasaki, H. (1992) *Reports on the R&D Program for the SPring-8 Beamline Construction ed.* by the JAERI-RIKEN SPring-8 Project Team, 83-87 (in Japanese).

Kamiya, N., Uruga, T., Yamaoka, M., Ueki, T. and Iwasaki, H. (1993) *Reports on the R&D Program for the SPring-8 Beamline Construction ed.* by the JAERI-RIKEN SPring-8 Project Team, 123-131 (in Japanese).

Sparks, C. J., Ice, G. E., Wong, J. and Batterman, B. W. (1982) *Nucl. Instrum. Methods* **194**, 73-78.

# 5. Performance of the Two-Dimensionally Tunable Focusing Monochromator

## 5.1. Bending properties and versatility of the curvature

Triangular bending monochromators with large asymmetric factors have been frequently used in the beamlines for protein crystallography at second-generation synchrotron radiation facilities. One of the major characteristics of this type of monochromator is its tunability in a certain range of X-ray energies. The present study is significant because it realizes tunability in the two-dimensionally focusing monochromator (Kawano & Kamiya, 1996).

### 5.1.1. Sagittal direction

The shape and versatility of the curvature can be precisely measured with a three-dimensional contour measurement apparatus (MP2000, Raytex Company, Ltd.) due to the small radius of sagittal curvature in the present monochromator. Fig. 19 (a) shows the observed central profiles of the monochromator in the sagittal direction with several values of $T_s$ rotation (see Fig. 13), and with $T_m$ rotation set to zero. (Hereafter, the number of rotations for $T_s$ and $T_m$ screws is also denoted by $T_s$ and $T_m$, respectively). In this measurement, the monochromator is first fully bent to a maximum value of $T_s = 90$. The averaged radius of curvature near the center (±1 mm) was calculated to be 0.54 m with an RMSD of 0.03 μm. The screws are then loosened to $T_s = 0$ and fastened to $T_s = 90$. Fig. 19 (b) clearly shows that this bending

mechanism gives excellent reproducibility in the radius of sagittal curvature of the monochromator.

### 5.1.2. Meridional direction

The central profiles of the monochromator in the meridional direction as measured by MP2000 are shown in Fig. 20 under the same measurement conditions as those of the above experiment. At $T_s = 90$ and $T_m = 0$, the entire contour plot of the crystal surface is shown in Fig. 21.

MP2000 is incapable of measuring the central traces in the meridional direction due to the large radii of meridional curvature. In order to determine them, an experimental setup was constructed, as shown in Fig. 22. Mo $K\alpha_1$ X-rays illuminated the present two-dimensionally focusing monochromator after passing through a 0.2 (horizontal) × 0.5 mm (vertical) XY slit. Intensity profiles of the X-rays reflected from the monochromator were measured with a silicon (111) crystal analyzer mounted on a $\theta/2\theta$ goniometer (MAC Science Company, Ltd.) in a (+,+) configuration. The measurements were carried out as a function of $T_m$ while varying the monochromator position in the meridional direction at intervals of 2 mm.

First, a silicon block was used to confirm the accuracy of this experimental setup. As shown in Fig. 23, the movement of the monochromator in the meridional direction caused angular changes, however, the deviations were considered to be small compared with the required accuracy (see Fig. 24).

Second, the two-dimensional focusing monochromator was mounted and the resultant data were corrected by the calibration data obtained using a silicon block.

Prior to the measurement, the monochromator was bent in the sagittal direction by $T_s$ = 90.

Fig. 25 shows a DuMond diagram (see Appendix B) of this experiment. The Mo $K\alpha_1$ radiation spread over 0.0003 Å in wavelength ($\Delta\lambda/\lambda = 4\times10^{-4}$). All of the intensity profiles were measured with an angular width of about 0.012° (hatched area in Fig. 25) in terms of full width at half-maximum (FWHM). The emergence angle ($\omega_h$) of the monochromator was estimated to be similar to the observed value since the wavelength spread of Mo $K\alpha_1$ radiation was too small to account for the large width observed. Considering the asymmetric factor ($b = 2.1$) under this experimental condition, the acceptance angle ($\omega_o$) of the monochromator is calculated to be 0.006°, which is two times larger than the theoretical width for a perfect crystal monochromator in the wavelength spread of Mo $K\alpha_1$ radiation. The increase in the acceptance angle may be due to the bending of the monochromator with a small radius of sagittal curvature.

The evaluated peak positions are plotted in terms of $\theta$ of the $\theta/2\theta$ goniometer (Fig. 24 (a)). The peak positions varied linearly with the position of the incident X-rays on the two-dimensionally bent monochromator. This corresponds to an angular variation of the monochromator surface. The observed slope of each line, $\Delta\theta/\Delta x$, is related to the radius of meridional curvature $R_m$ by

$$\frac{\Delta\theta}{\Delta x} = \frac{1}{R_m} . \tag{19}$$

The positive and negative slopes correspond to the concave and convex shapes, respectively. The averaged radii of curvature evaluated with a least squares fit to the straight lines were over 61 m for the concave shapes, and over 110 m for the convex

ones. These changes in the curvatures were experimentally confirmed to be reversible, as shown in Fig. 24 (b). Although deviations of the $R_m$ values are relatively large at $T_m = 0$ and -1, they are mainly due to the small values of the slopes compared with the positional errors of the measured intensity profiles.

## 5.2. Focusing of high-energy X-rays

The focusing capabilities of the monochromator for high-energy X-rays were carefully examined using the BL-15B at the PF. After being shaped with an XY slit having horizontal and vertical opening widths of 1.5 and 1.0 mm, respectively, white X-rays were incident upon the monochromator mounted on a Huber goniometer (Fig. 26). The X-ray energy corresponding this goniometer angle was 37.7 keV using the standard angle for the $K$ absorption edge of barium ($E$ = 37.5 keV) as reference. Under the focusing conditions of $T_s = 90$ and $T_m = 0$, the X-rays reflected by the monochromator were recorded on industrial X-ray films (IX80, Fuji Film Company). Five photographs were taken at positions 2.64, 3.49, 4.11, 4.45 and 4.89 m from the monochromator. The photographs were analyzed using a densitometer (Model 1010M Micro-D, Perkin-Elmer Company), and the measured horizontal and vertical FWHM beam sizes are plotted in Fig. 27.

The beam size observed in the sagittal direction decreases monotonically without any clear focal points in the given range of distance. It is anticipated that the focal point may be outside the experimental hutch of the BL-15B, and so it is inferred that the present condition of $T_s = 90$ is insufficient for converging X-rays at the same position in the two directions. This inference is consistent with the results reported above that the radius of sagittal curvature of 0.54 m at $T_s = 90$, determined

from three-dimensional contour measurements, is larger than the designed value of 0.42 m (see Table 2).

On the other hand, the beam size in the meridional direction exhibits a concave feature over the experimental distances of 2.64 to 4.89 m. Assuming a function of the second order, the result of a least squares fit indicates a focal point at 3.96 m, which is 0.5 m shorter than the designed value of 4.45 m. The estimated minimum focal spot size is 0.22 mm with a focal depth of about ± 0.5 m.

Fig. 28 shows five contour maps of reflected X-rays. In the cases of short distances (Figs. 28 (a) to (c)), the observed profiles include two peaks in the horizontal direction. The double-peak distribution tends, however, to disappear in the other two contour maps (Figs. 28 (d) and (e)). As shown in Fig. 28 (e), the X-ray beam originally of 1.5 × 1.0 mm area was successfully converged to 0.22 × 0.27 mm in a quasi-isotropic profile using the present monochromator. The beam profile attained should, however, be considered as an overlap of the two components observed at a short distance, as shown in Fig. 28(a).

With reference to the beamline specifications, the FWHM source sizes of BL-15B are 0.80 (horizontal) and 0.37 mm (vertical) (Photon Factory Activity Report #10, 1992). The expected focal spot size is calculated to be 0.11 × 0.05 mm based on the asymmetric factor of 8.27 of the present monochromator. The observed focal size in the meridional direction is, however, two times larger than the calculated value. Furthermore, the observed focal length differs from the designed one by 0.5 m, and the estimated focal depth seems to be wider than expected.

These discrepancies can be explained as follows. Based upon the simulations carried out, as well as the observed distribution of the X-ray intensity profiles, it is

assumed that the active area of the monochromator surface consists of three parts in the meridional direction: one is the central area which is more cylindrical than toroidal, and the other two are the toroidal areas adjacent to it. The discrepancies should also be considered in terms of chromatic aberration (see Appendix C) of a focusing monochromator having such a large asymmetric factor as in the present case. Applying the formulation recently derived by Takeshita (1995) to the present monochromator, the focal size in the meridional direction is calculated to be 0.18 mm when the radius of meridional curvature is assumed to be 300 m for the two toroidal areas. This implies that the expected focal size in the meridional direction is much larger than the value calculated only due to the use of the asymmetric factor.

Fig. 29 illustrates the situations considered above. The double-component properties observed at position (a) disappear at position (c). The smallest beam size could be realized at the apparent focal point (b). This figure also visually explains the findings that the measured focal length is different from the designed value, and that the beam size is larger than the expected one. Furthermore, the depth of focus could be broader than that expected with an ideally curved monochromator.

To evaluate the reflectivity and the flux gain of the present two-dimensional focusing monochromator, another set of 4 photographs was taken after substituting the monochromator with a flat silicon (111) block ($\alpha$ = -0.70°, $b$ = 1.61) (Figs. 30 and 31). The evaluation was made using two photographs taken at 4.89 m; one with the monochromator and the other with the silicon block. The optical density was deduced by integrating the recorded densities over the entire region of the beam area.

There exist some differences in the experimental conditions for the Si block and the present monochromator (Table 3). Integrated intensity was corrected based on these differences. The integrated intensities obtained from the optical densities

are 2863.35 and 135.98 for the silicon block and the present monochromator, respectively. The expected ratios of integrated intensities of the silicon block and the present monochromator are 2:1 from X-ray exposure time, 1: 0.163 from X-ray absorption with aluminum attenuators, and 5.84 : 2.71 from acceptance angle of the monochromators. The difference in the PF storage ring currents is ignored.

Table 3 : Difference in experimental conditions of the Si block and the present monochromator.

| | exposure time (sec) | Al attenuator (mm) | ring current (mA) | $\omega_0$ (mrad) |
|---|---|---|---|---|
| Si block | 20 | 10 | 281 | $5.84 \times 10^{-3}$ |
| 2D monochromator | 10 | 20 | 310 | $2.71 \times 10^{-3}$ |

The ratio for the aluminum attenuator was obtained from the absorption coefficient ($I_1/I_2 = \exp(-\mu x_1)/\exp(-\mu x_2)$). $\mu$ is the absorption coefficient calculated from $\mu/\rho = 0.672$ (at $\lambda = 0.33$ Å) and $\rho = 2.70$ (at 20 °C). $\omega_s$ of Si block for Cu $K\alpha_1$ ($\lambda = 1.54$ Å) is 7.395 arcsec (0.036 mrad).

The corrected ratio of the optical density of the present monochromator to that of the silicon block was 3/5. The flux gain evaluated from the peak heights observed in the two photographs taken at 4.89 m for the present monochromator and the silicon block was as high as 10.

As already mentioned, the angular acceptance width of the present monochromator was increased by bending in the sagittal direction. Following the increase in the angular acceptance width, it may be assumed that the reflectivity of the monochromator is reduced, that is, the integrated intensity of the reflected X-rays with the present monochromator is similar to the theoretical value obtained for a

perfect crystal. If this assumption is valid, since the theoretical ratio acceptance angles ($\omega_0$ in Table 3) of the present monochromator and the silicon block is 1/2 under the conditions for the focusing experiments, the monochromator developed in this work can be regarded as one which loses no reflectivity in its two-dimensional bending mechanism. The flux gain recalculated based on the same assumption is 21, which is in good agreement with that obtained from the size demagnification from the incident X-ray beam (1.5 × 1.0 mm) to the focused one (0.22 × 0.27 mm).

The energy resolution of the present monochromator was not measured. However, it was estimated as $2 \times 10^{-3}$ under the conditions of the focusing experiments based upon the acceptance angle of the two-dimensionally bent monochromator of 0.006°.

## 5.3. Oscillation photograph of protein crystal

An oscillation photograph of a tetragonal crystal of hen egg white lysozyme was taken using high-energy X-rays focused with the monochromator, as shown in Fig. 32. A crystal of 1.2 × 1.2 × 0.5 mm size was mounted on a Huber precession and rotation chamber. The c-axis was set near the spindle axis. The chamber was located 4.45 m behind the monochromator, and an imaging plate (BAS-UR, Fuji Film Company) was used for recording the diffraction pattern.

The oscillation angle and the exposure time were 0.1° and 5 min, respectively, at a PF storage ring current of 290 mA. The relatively long exposure time was required partly because of the low brilliance of the X-rays generated by the PF bending magnet at 37.7 keV and partly because of the small horizontal and vertical acceptance widths of 41 and 27 μrad of the present monochromator. In order to

obtain a diffraction image of good quality with high-energy X-rays, well-focused and highly monochromatic X-ray beam should be used since the diffraction pattern of the high-energy X-rays is spatially reduced. Because two neighboring spots were distinctly separated in the horizontal direction with an interval of only 0.87 mm, as shown in Fig. 32, we can conclude that the present monochromator is sufficient for use in protein crystallography.

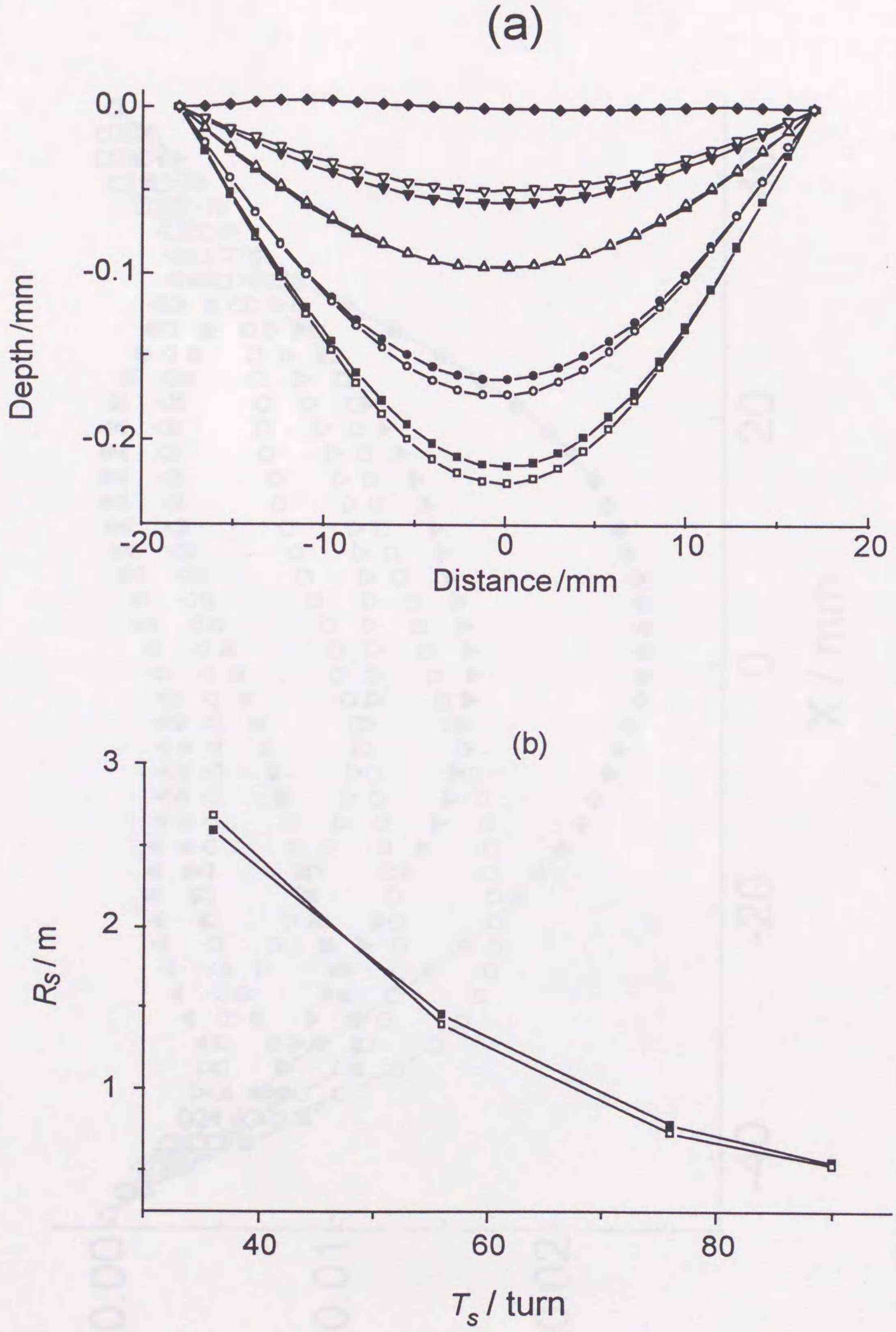


Fig. 19 : (a) Trace and versatility in sagittal direction. Profile measurements were carried out at 0.01 mm intervals at $T_s$ = 90 (■ : loosening, □ : fastening), 76 ( ●, ○), 56 (▲, △), 36 (▼, ▽) and 0 (◆). Each symbol represents one data point selected from a set of 140 data points for clarity. Distance from center and depth from a standard point (18 mm from center) are indicated. (b) Reproducibility of the radius of sagittal curvature. ■ : loosening, □ : fastening.

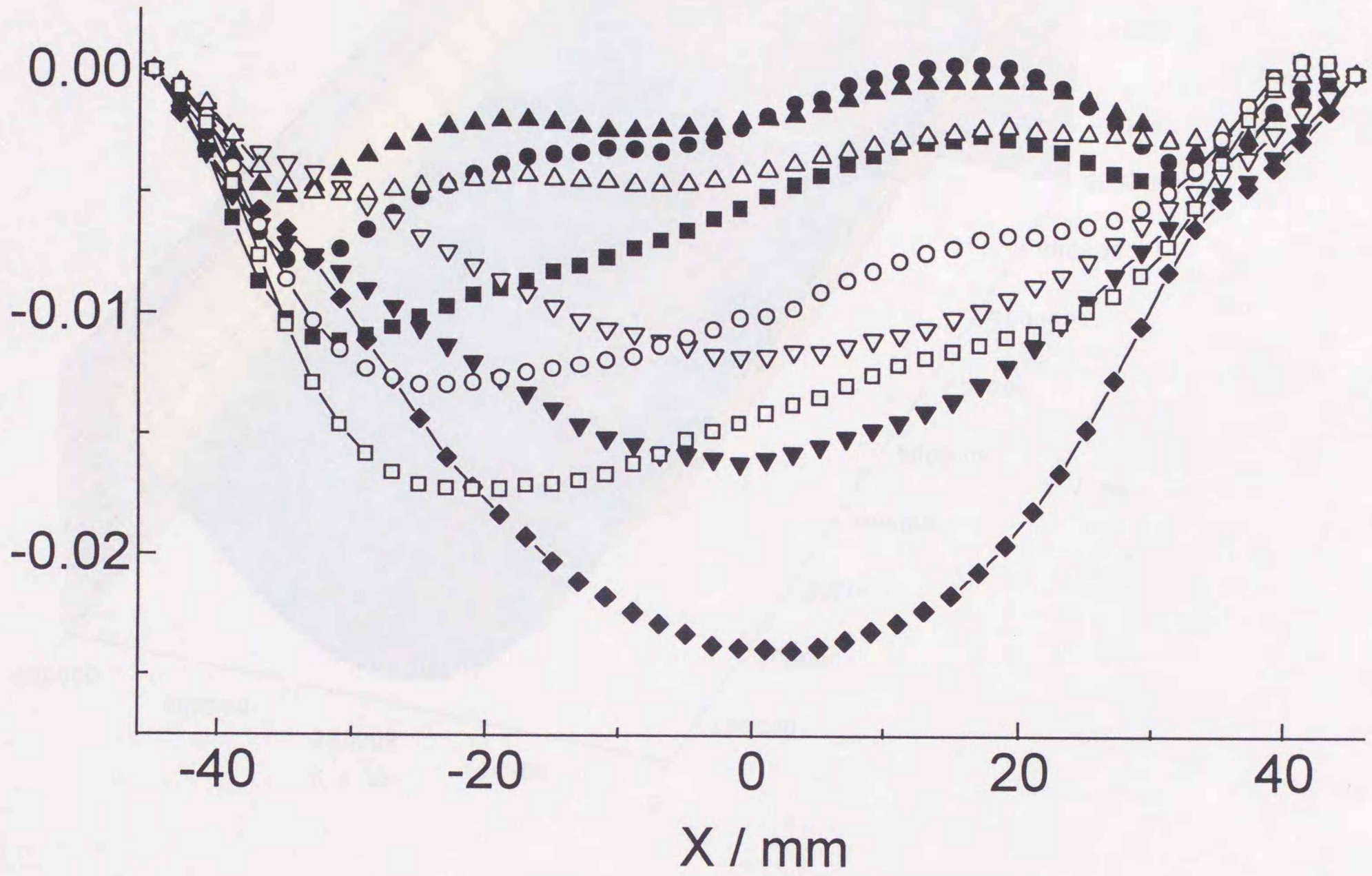


Fig. 20 : Trace and versatility in meridional direction. Profile measurements were carried out at 0.01 mm intervals at $T_s$ = 90 (■: loosening, □: fastening), 76 (●, ○), 56 (▲, △), 36 (▼, ▽) and 0 (◆). Each symbol represents one data point selectd from a set of 200 data points for clarity. Distance from center and depth from a standard point (45 mm from center) are indicated.

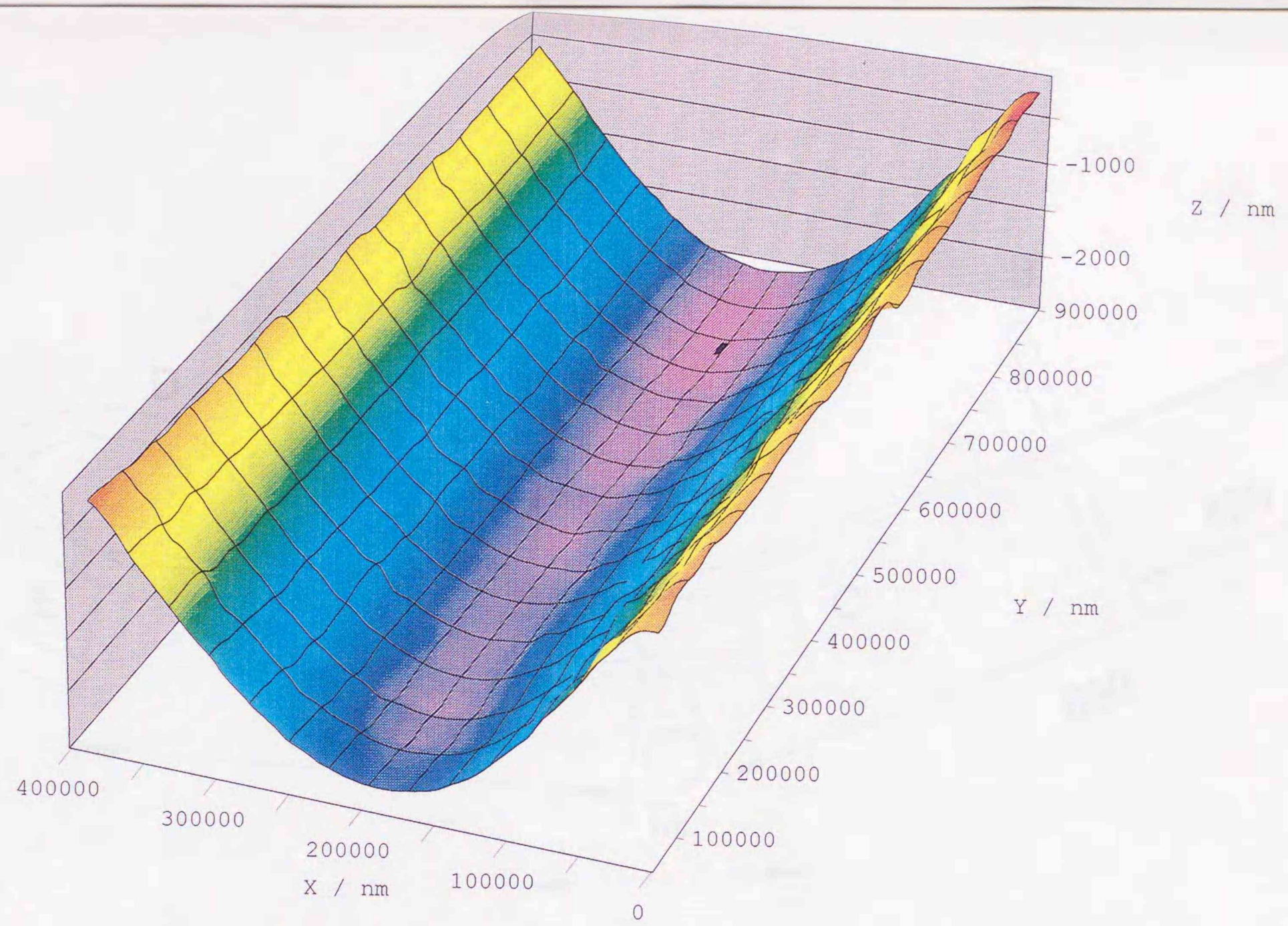


Fig. 21 : The entire contour plot of monochromator surface. This is measured at $T_s$ = 90 and $T_m$ = 0, and in 0.2 mm intervals in both directions.

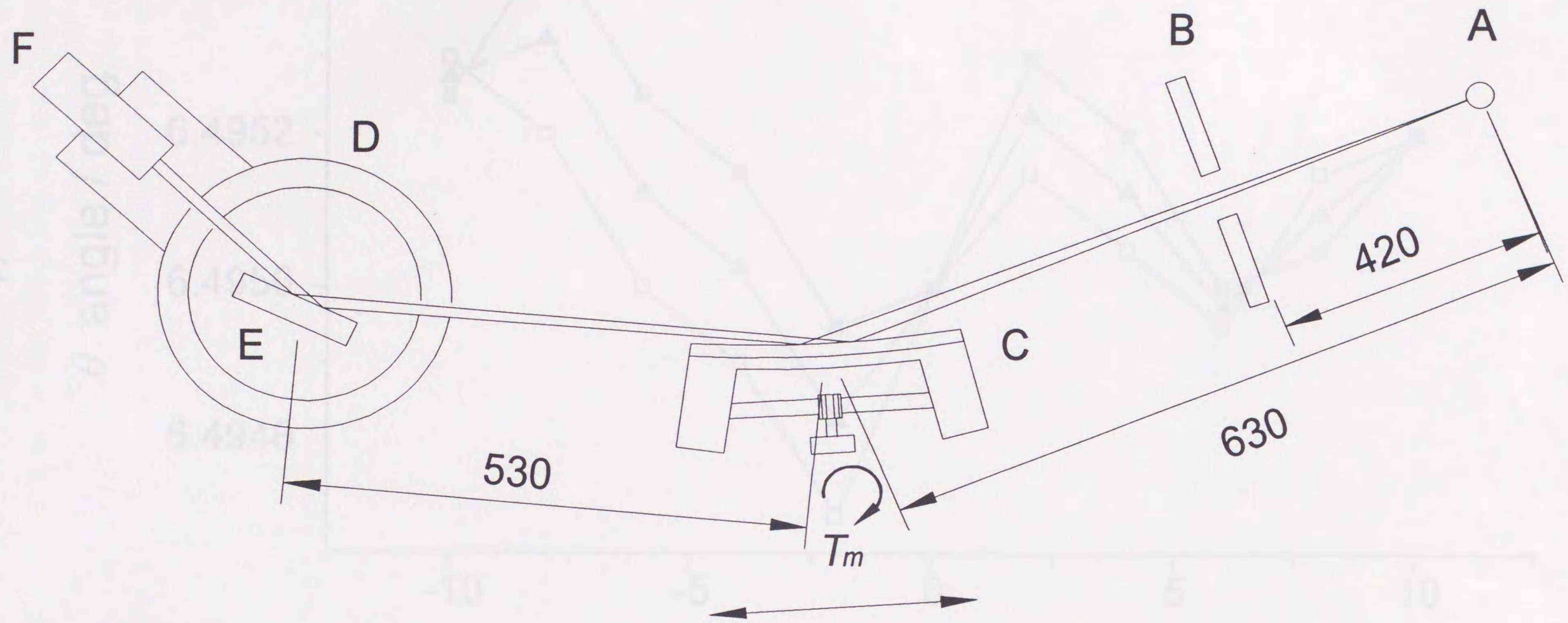


Fig. 22: Experimental setup for X-ray measurements. *A*: X-ray point source (0.2 x 0.2 mm), *B*: XY slit, *C*: two-dimensional focusing monochromator on a sliding stage, *D*: $\theta/2\theta$ goniometer, *E*: Si crystal analyzer, and $T_m$: meridional bending screw. Distances are expressed in mm.

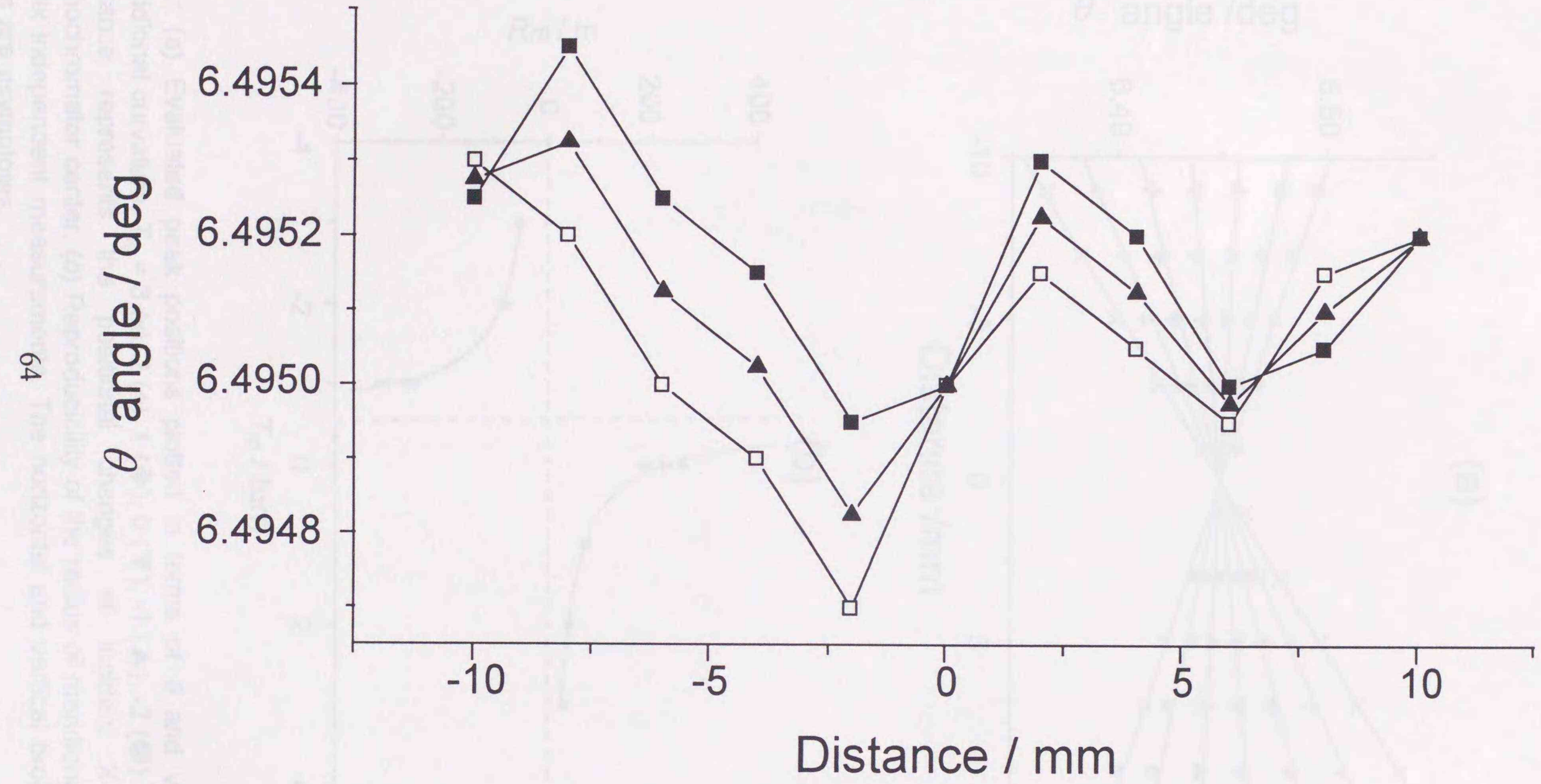


Fig. 23 : Evaluated peak positions plotted in terms of $\theta$ and versatility of distance which is represented by the positional changes of incident X-rays from monochromator center.

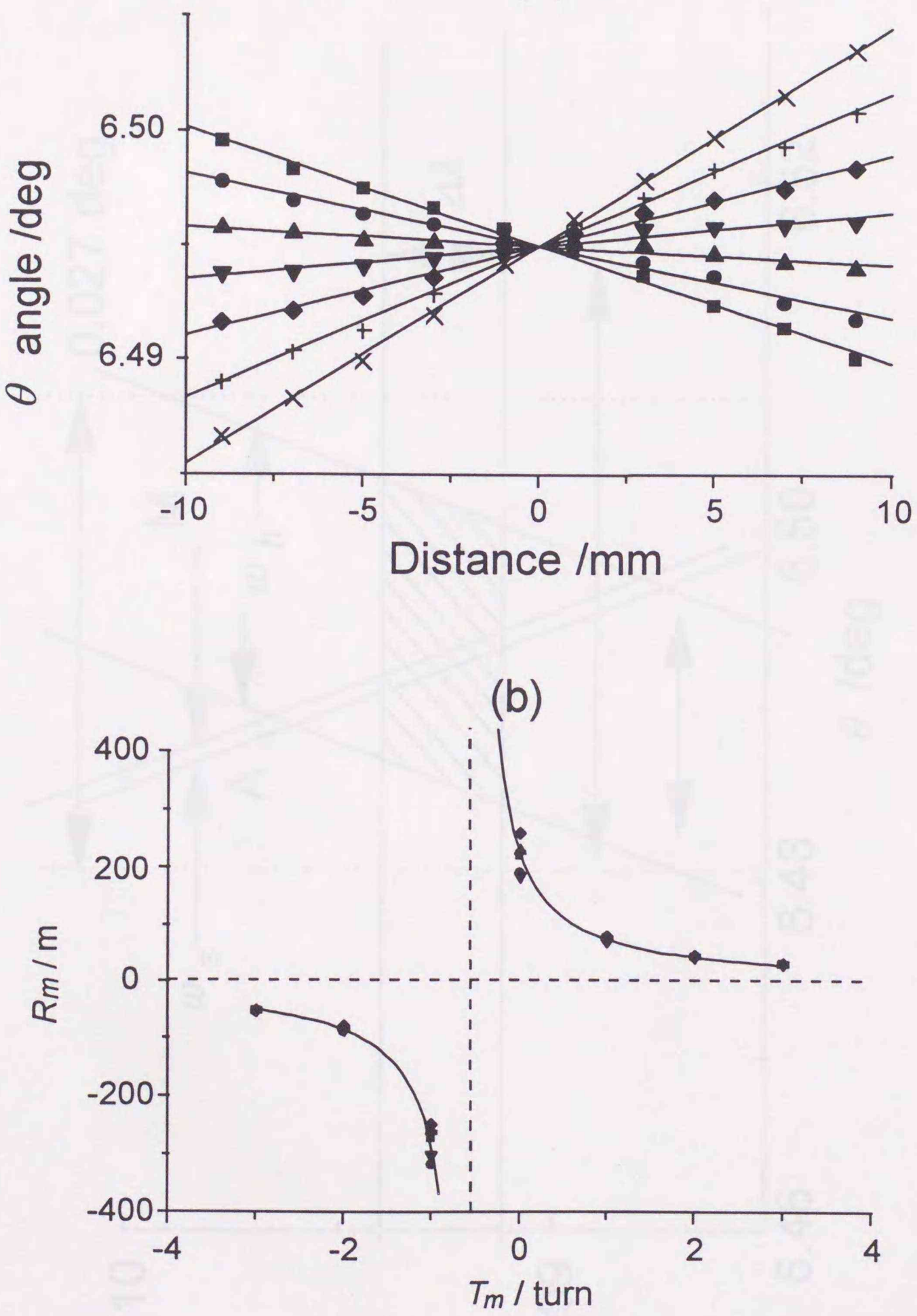


Fig. 24 : (*a*) Evaluated peak positions plotted in terms of $\theta$ and versatility of meridional curvature. $T_m$ = 3 (x), 2 (+), 1 (◆), 0 (▼), -1 (▲), -2 (●) and -3 (■). Distance represents the positional changes of incident X-rays from monochromator center. (*b*) Reproducibility of the radius of meridional curvature in six independent measurements. The horizontal and vertical broken straight lines are asymptotes.

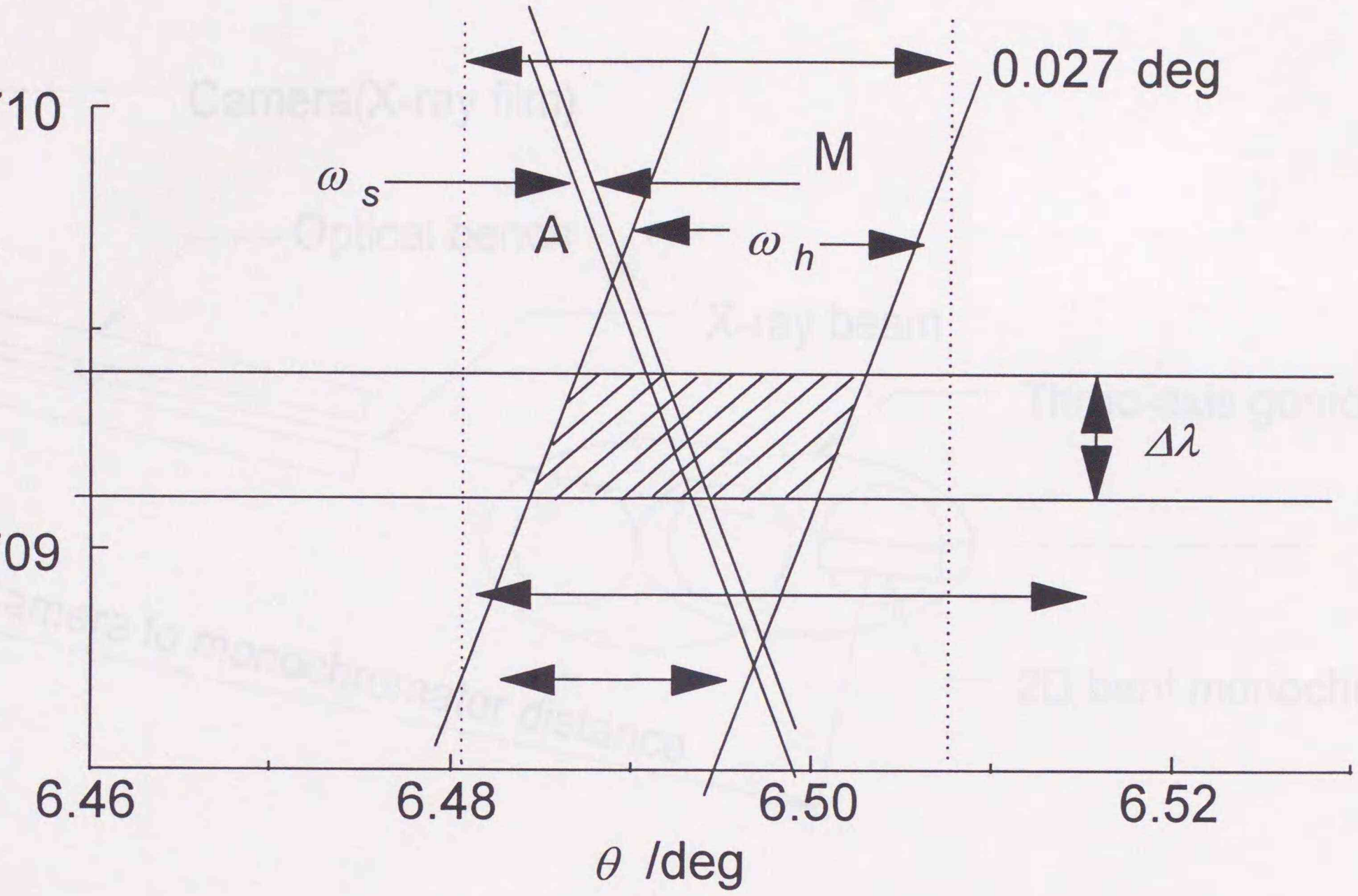


Fig. 25 : DuMond diagram of X-ray experiments. $\Delta\lambda$: wavelength spread of Mo $K\alpha 1$ radiation, $\omega_h$: angular emergence width of two-dimensional focusing monochromator in the meridional direction, $\omega_s$: intrinsic width of Bragg reflection of Si (111) crystal analyzer on a $\theta/2\theta$ goniometer. The domain (*A*) of the analyzer moves following the $\theta$ axis rotation of the goniometer, and that of the monochromator (*M*) shifts its angular position following its translation in the meridional direction. The broken lines indicate angular width of the incident X-rays on the monochromator.

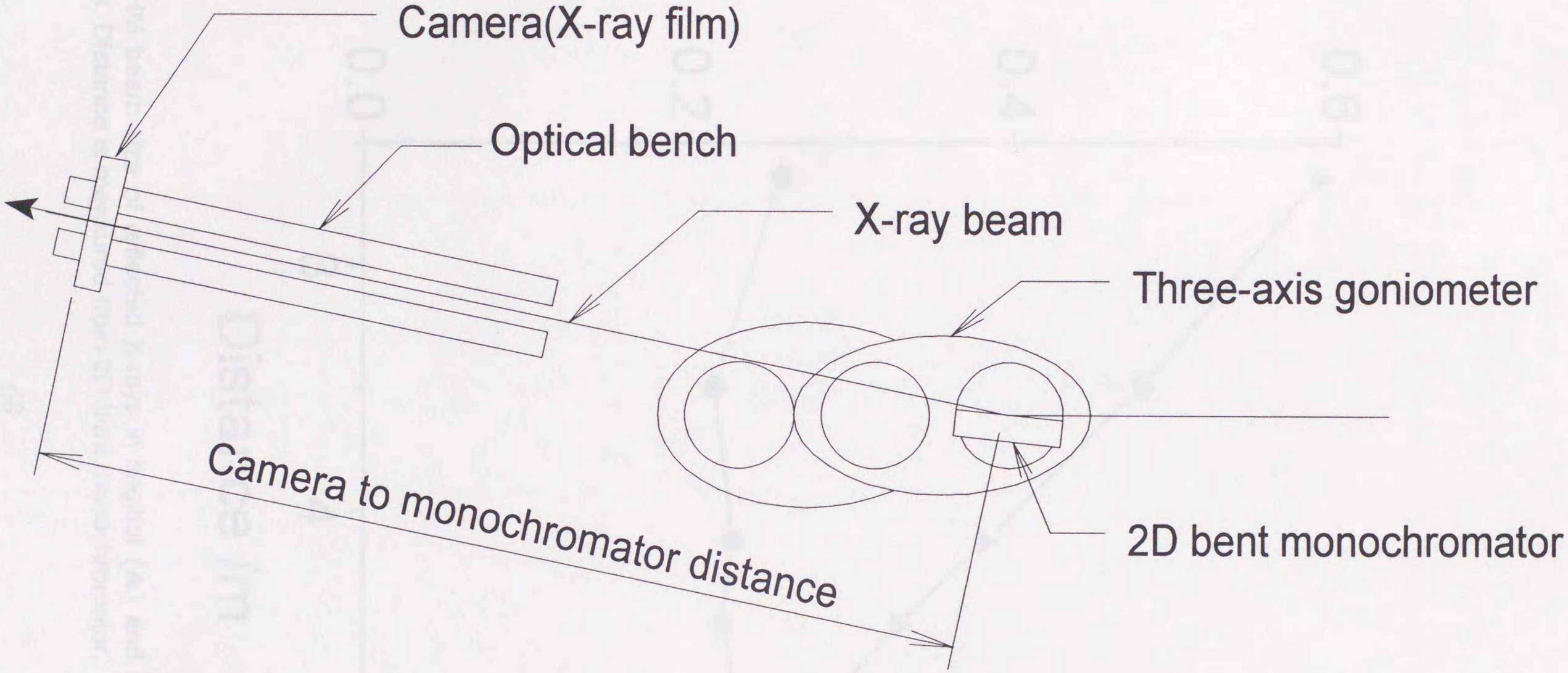


Fig. 26 : Experimental setup for X-ray measurements.

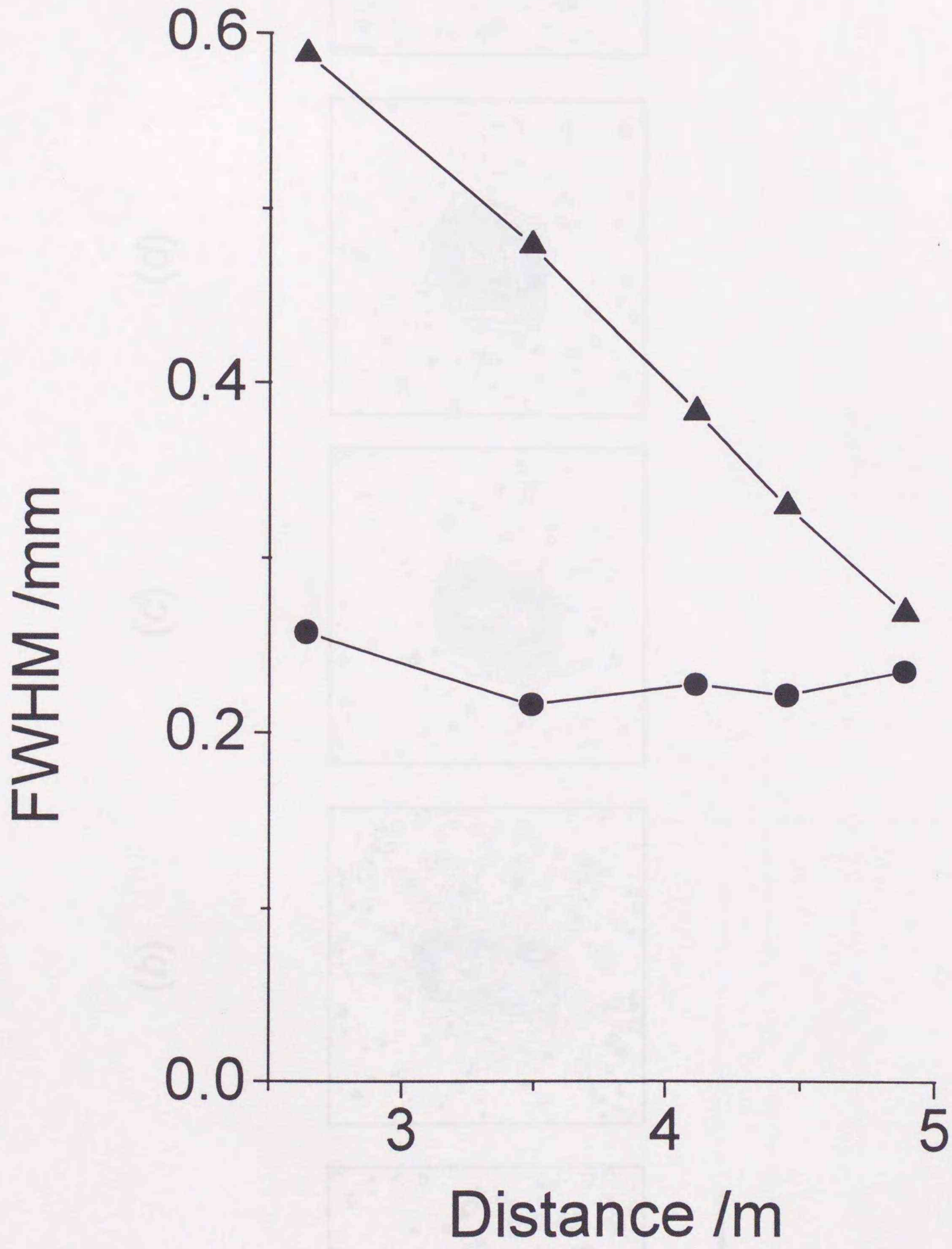


Fig. 27 : FWHM beam size of reflected X-rays in sagittal (▲) and meridional (●) directions. Distance is measured from 2D bent monochromator.

(*a*) (*b*) (*c*) (*d*) (*e*)

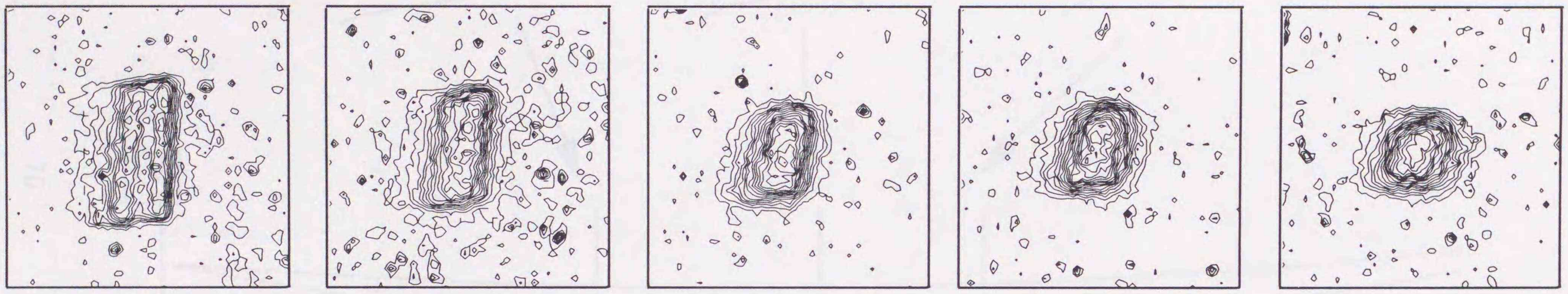

Fig. 28 : Contour maps of reflected X-rays using 2D-bent monochromator. (*a*) is exposed at 2.64 m from the monochromator. (*b*) is at 3.49 m. (*c*); 4.11 m. (*d*); 4.45 m. (*e*); 4.89 m. The contours start from an optical density of 0.2 with 0.05 intervals. Scale bar under (*a*) indicates 1 mm.

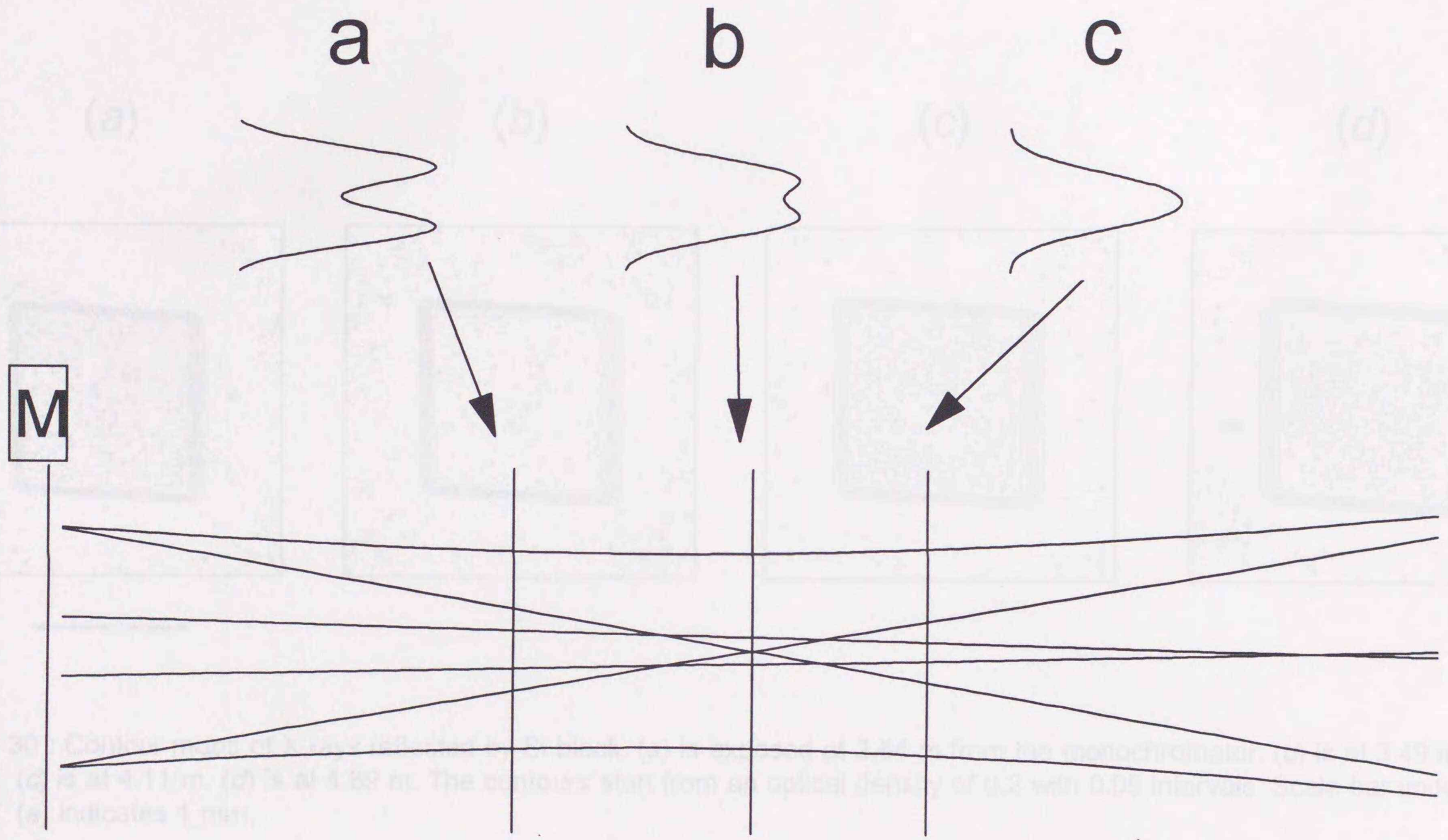


Fig. 29 : Focusing scheme in the meridional direction. The monochromator (*M*) is represented by a line for clarity. Profiles *a-c* are expected at the indicated positions.

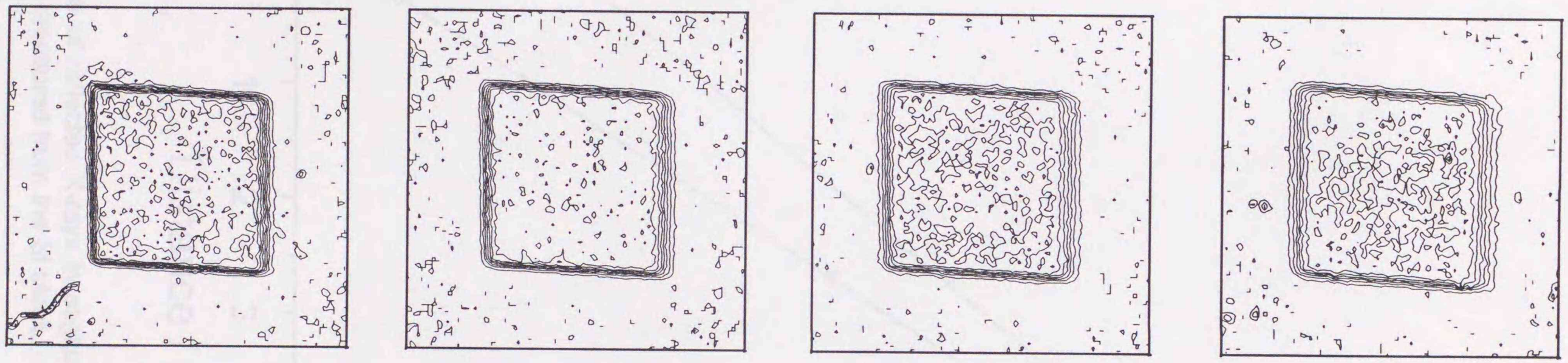


Fig. 30 : Contour maps of X-rays reflected by Si block. (*a*) is exposed at 2.64 m from the monochromator. (*b*) is at 3.49 m. (*c*) is at 4.11 m. (*d*) is at 4.89 m. The contours start from an optical density of 0.2 with 0.05 intervals. Scale bar under (*a*) indicates 1 mm.

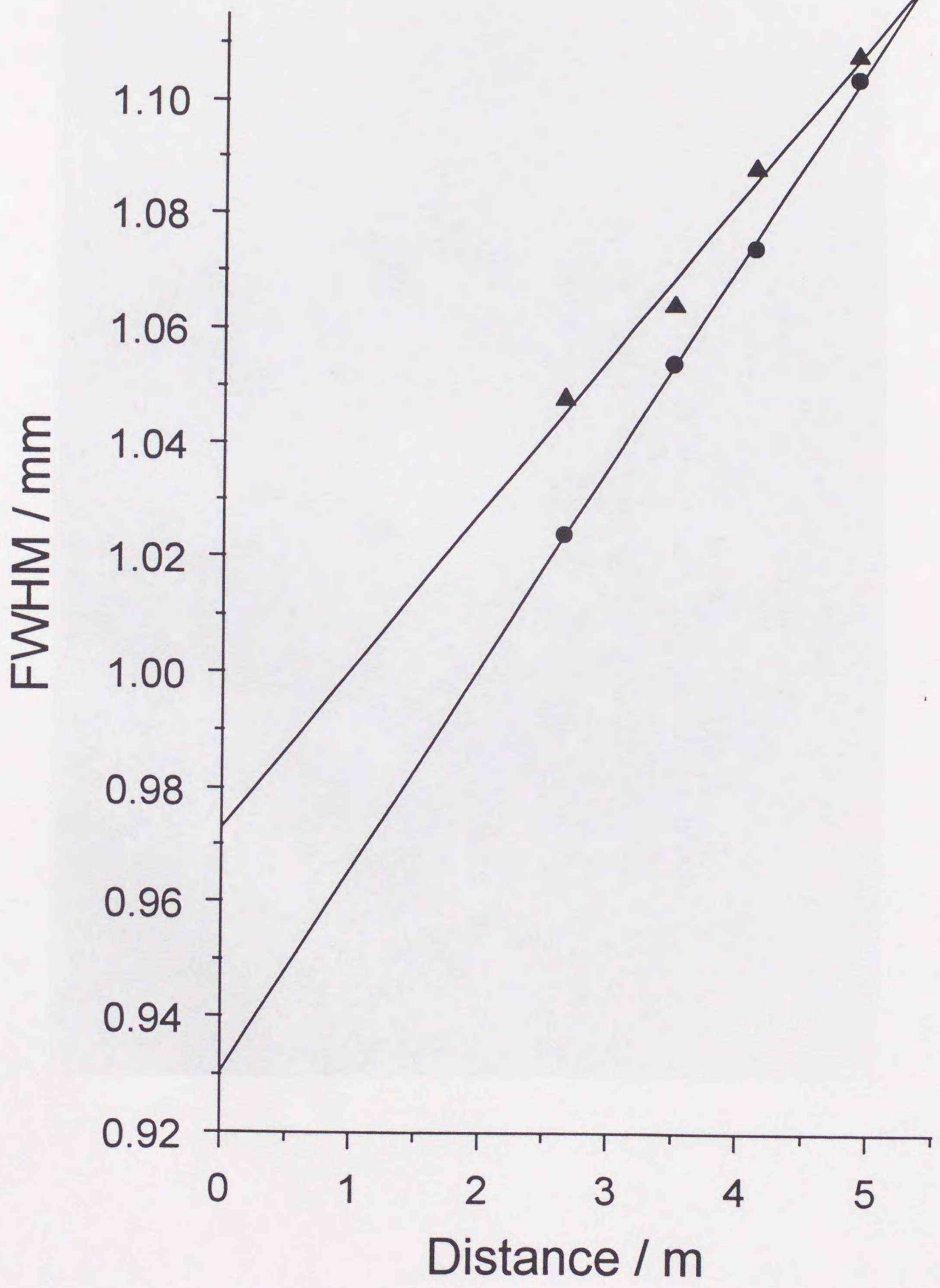


Fig. 31 : FWHM beam size of reflected X-rays in sagittal (▲) and meridional (●) directions. Distance is measured from the Si block.

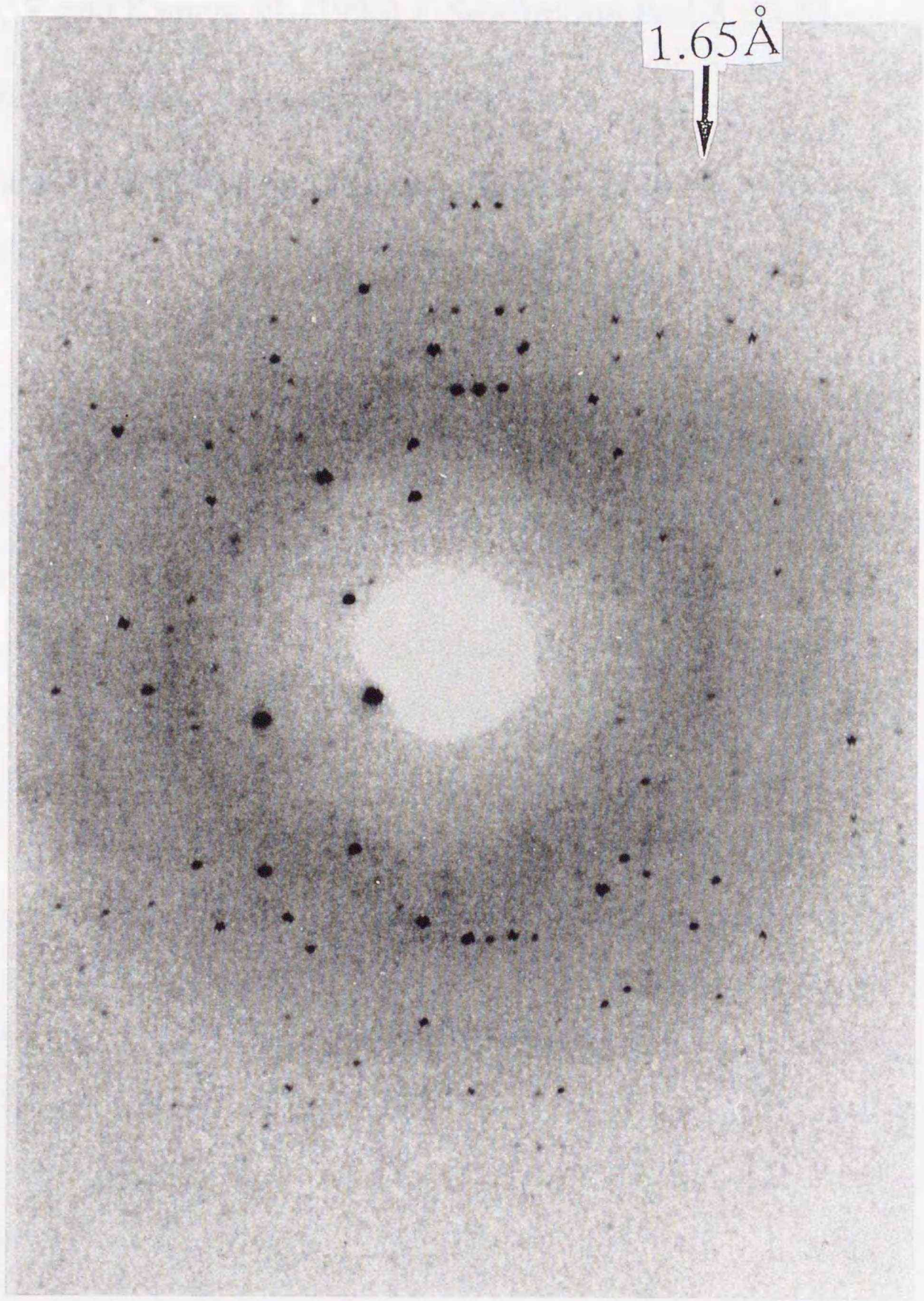


Fig. 32 : Oscillation photograph of hen egg-white lysozyme crystal using 37.7 keV X-rays. The sample crystal belongs to a tetragonal system (space group, $P4_32_12$) with cell dimensions of $a$ = 79.1 and $c$ = 38.0 Å. Distance from the sample crystal to the imaging plate is 100 mm. The arrow indicates a spot of 1.65 Å resolution.

# References

Kawano, Y. and Kamiya, N. (1996) *J. Synchrotron Rad.* **3**. 53-61.

Photon Factory Activity Report #10 (1992) R-30.

Takeshita, K. (1995) *Rev. Sci. Instrum.* **66**, 2238-2240.

# 6. Conclusion and Future Prospects

I have developed a two-dimensionally tunable focusing monochromator for use with high-energy X-rays from undulators of third-generation synchrotron radiation facilities. This monochromator is suitable for use in protein crystallography due to its tunability and excellent performance in terms of small focal size, high flux gain and adequate energy resolution.

Based on the results obtained in this work, I am designing a monochromator system for a hypothetical undulator beamline at the SPring-8. The design parameters are shown in Table 4 (Kawano & Kamiya, 1996). The system will consist of three individual monochromators and will cover the energy range of 20 - 40 keV. The distance between the source point and the monochromator system will be arbitrarily selected from a standard position at which the monochromator system can be set in the SPring-8 experimental hall. In designing the monochromator system, one of the major problems is how large the area available for setting the experimental equipment will be, which will affect the range of acceptable focusing distances. Considering the conditions of the SPring-8 experimental hall, I choose 6 - 10 m as the distances between the monochromator system and the focal point, thus suppressing tangential distances less than 1.6 m from the focal points to the beamline.

In order to realize the monochromator system on the SPring-8 beamline, however, sufficient measures must be taken to cope with the high heat-load problem. The cryogenic cooling technique developed in the European Synchrotron Radiation Facility may be used. There are two possibilities for utilizing this technique in the present two-dimensionally tunable focusing monochromator, an indirect cooling of a

very thin wafer and a direct cooling of a relatively thick one as described in this dissertation. In the former, a thin wafer will be made as one body on a tablelike silicon block (Rogers, *et al.* 1995), and liquid nitrogen will be made to flow through the table legs. In the latter, a relatively thick wafer and a tablelike silicon block with liquid nitrogen flow will be individually prepared, and then bonded (Yamaoka, Freund, Ohtomo & Krumrey, 1995). For bonding, the epoxy glue used in this work is not applicable because of its poor resistance to synchrotron radiation.

Table 4 : Design parameters for a hypothetical monochromator system.

| | | | |
|---|---|---|---|
| distance from source to monochromator ($p$) | 36 m | | |
| distance from monochromator to focus ($q$) | 6 - 10 m | | |
| range of X-ray energy | 20 - 40 keV | | |
| **monochromator** | **I** | **II** | **III** |
| individual energy range | 20.0 - 25.3 | 25.3 - 31.9 | 31.9 - 40.0 keV |
| Bragg angle ($q$) of Si (111) | 5.67 - 4.49 | 4.49 - 3.56 | 3.56 - 2.83 deg |
| asymmetric angle ($\alpha$)* | -3.21 | -2.54 | -2.01 deg |
| asymmetric factor ($b$)* | 3.6 - 6.0 | 3.6 - 6.0 | 3.6 - 5.9 |
| radius of meridional curvature ($R_m$)* | 233 - 269 | 294 - 339 | 371 - 427 m |
| radius of sagittal curvature ($R_s$)* | 1.55 - 0.81 | 1.22 - 0.64 | 0.97 - 0.52 m |

*) definitions are given in the text.

Although these ideas must be simulated by the finite element method with the ANSYS program from the viewpoints of bending properties and heat-load deposition, I believe that the designed two-dimensionally tunable focusing monochromators can be used in the SPring-8 undulator beamlines.

The X-ray intensity usually obtained at a sample position on the bending magnet beamline of the PF is about $10^{10}$ photons/sec at an X-ray wavelength of 1 Å (12.4 keV) after collimating with a 0.1 mm slit.

The X-rays are converged by a two-dimensionally focusing system consisting of a total reflection mirror and a triangular bending monochromator. The brightness of 40 keV X-rays (about 0.31 Å wavelength) from the bending magnet source is 1/100 that of 12 keV X-rays. Therefore, the X-ray intensity obtained from the bending magnet beamline at 40 keV is about $10^8$ photons/sec.

In contrast, the intensity of X-rays emitted from the undulator of the SPring-8 at 40 keV will exceed $10^{14}$ photons/sec. If high-energy X-rays are converged by the present two-dimensionally focusing monochromator, the focal spot size becomes about 0.2 mm × 0.3 mm. The intensity of X-rays passing through a 0.1 mm collimator may reach $10^{13}$ photons/sec at the sample position. Therefore, the intensity of the high-energy X-rays obtained from the SPring-8 undulator beamline may be $10^5$ times larger than the intensity obtained from the PF bending magnet beamline.

Assuming that the intensities are equal for the incident 40 and 12 keV X-rays, the diffraction intensity of 40 keV X-rays becomes 1/10 that of 12 keV X-rays. When a diffraction experiment is performed using 40 keV X-rays from the SPring-8 undulator and the present monochromator, the diffraction intensity is $10^4$ times larger than that measured with 12 keV X-rays at the PF. If the ratio of the diffraction intensity to the crystal volume is taken into consideration, the diffraction intensity obtained with a 0.1 mm cubic crystal and the 12 keV X-rays at the PF may equal that obtained with a several tens of microns crystal and the 40 keV X-rays from the SPring-8 undulator using the present monochromator.

When high-energy and high-intensity X-rays achieved by the development of the present monochromator are used, systematic errors in the measured diffraction data may be reduced, which originate from X-ray absorption by the sample crystal, the solvent for crystallization and the glass capillary. The quality of isomorphous data for MIR phasing and anomalous dispersion data for OAS phasing can be improved.

Moreover, radiation damage to the crystal may be decreased by decreasing the amount of X-rays absorbed by the crystal. In addition, the accessible elemental absorption edges are extended to the *K* edges of biologically useful molybdenum (20 keV), cadmium (26.7 keV), iodine (33.2 keV), and xenon (34.6 keV), and the *L* edge of uranium (21.8 keV). The expansions of the heavy atom compounds may facilitate the preparations of heavy atom derivative crystals. As discussed above, the development of the present monochromator will contribute much to the elucidation of the structure of biological macromolecules in the near future.

# References

Kawano, Y. and Kamiya, N. (1996) *J. Synchrotron Rad.* **3**. 53-61.

Rogers, C. S., Mills, D. M., Lee, W.-K., Knapp, G. S., Homberg, J., Freund, A., Wulff, M., Rossat, M., Hanfland, M. and Yamaoka, H. (1995) *Rev. Sci. Instrum.* **66**, 3493-3499.

Yamaoka, H., Freund, A. K., Ohtomo, K. and Krumrey, M. (1995) *Rev. Sci. Instrum.* **66**, 2092-2094.

# 7. Appendices

## 7.1. Appendix A - Asymmetrically cut monochromator

In a perfect single crystal, X-ray diffraction occurs based on a dynamical theory. When X-rays reach the crystal surface at an angle $\theta_B$, the acceptance angle $\omega_0$ and the emergence angle $\omega_h$ (Fig. 33) are

$$\omega_0 = \sqrt{|b|}|\psi'_h|/2\sin 2\theta_B, \tag{20}$$

$$\omega_h = |\psi'_h|/2\sqrt{|b|}\sin 2\theta_B, \tag{21}$$

where $\psi'_h$ is the Fourier element of crystal polarizability at an index $\boldsymbol{h}$ and $b$ is the asymmetric factor expressed by

$$b = \frac{\sin(\theta_B - \alpha)}{\sin(\theta_B + \alpha)}, \tag{22}$$

where $\alpha$ is the oblique-cut angle between the Bragg net plane and the crystal surface.

The angles $\omega_0$ and $\omega_h$ are usually between one and a few tens seconds. The relation between the emergence beam width $S_h$ and acceptance beam width $S_0$ (Fig. 33) is given by

$$S_0/S_h = |b|. \tag{23}$$

## 7.2. Appendix B - DuMond diagram

The DuMond diagram is generally used for estimating the performance of an X-ray optical system (Nakayama, *et al.* 1972; DuMond, 1937). In this method, the characteristics of an optical system are expressed in the wavelength ($\lambda$) - angle ($\theta$) space.

In Fig. 34, an example of the DuMond diagram is shown for the crystal monochromator characterization. A center curve of domain $C$ corresponds to Bragg's equation $\lambda = 2d\sin\theta$ ($d$ is lattice spacing). The width of the domain along the $\theta$ axis is equal to the reflection width $\omega$ of the crystal. When incident X-rays have a white spectrum and a divergence angle $\Delta\theta$, the X-rays are expressed by the domain XB parallel to the $\lambda$ axis. X-rays reflected by the crystal are expressed by the common part of these two domains C and XB. Since the characteristics of the X-rays in terms of angle and wavelength distribution are shown, this part is called the beam characteristic window.

In Fig. 35, the (+,+) configuration of a symmetrically cut monochromator is shown. Here the glancing angles of X-rays on the first and second crystals are $\theta_1$ and $\theta_2$, respectively. The constant angle $\Theta$ is

$$\theta_1 + \theta_2 = \Theta, \tag{24}$$

with

$$\mathrm{d}\theta_1 = -\mathrm{d}\theta_2. \tag{25}$$

In the DuMond diagram, the domains for the two monochromators are drawn, as shown in Fig. 36. The expression for the energy resolution of reflected X-rays is obtained from the beam characteristic window as,

$$\frac{\Delta E}{E} = \frac{\omega_1 + \omega_2}{\tan\theta_1 + \tan\theta_2}. \qquad (26)$$

The narrow beam characteristic window with $\Delta\lambda$ and $\Delta\theta$ is obtained without substantial slits.

## 7.3. Appendix C- Chromatic aberration

When the asymmetric diffraction geometry is used in an optical focusing system, the apparent focal size is larger than that obtained from the theory. Recently, it has been clarified that an increase in the focal spot size is due to chromatic aberration of the monochromator (Takeshita, 1995).

Considering an asymmetric Johann-type monochromator (see Fig. 37), the distances *OF* and *OS* are given by

$$OF = R_m\cos(\theta_B + \alpha), \qquad (27)$$

and

$$OS = R_m\cos(\theta_B - \alpha). \qquad (28)$$

For a polychromatic incident beam with a wavelength between $\lambda_1$ and $\lambda_2$, the X-rays from a point *S* are reflected at each point on the crystal by the corresponding Bragg angles with an angular spread of $\Delta\Theta = (b\text{-}1)\omega_0$. X-rays with different

wavelengths are focused at different points between $F_1$ and $F_2$. Therefore, the increase in the focal spot size due to chromatic aberration is represented by

$$F_1F_2 = R_m(b\text{-}1)\omega_0\sin(\theta_B + \alpha). \tag{29}$$

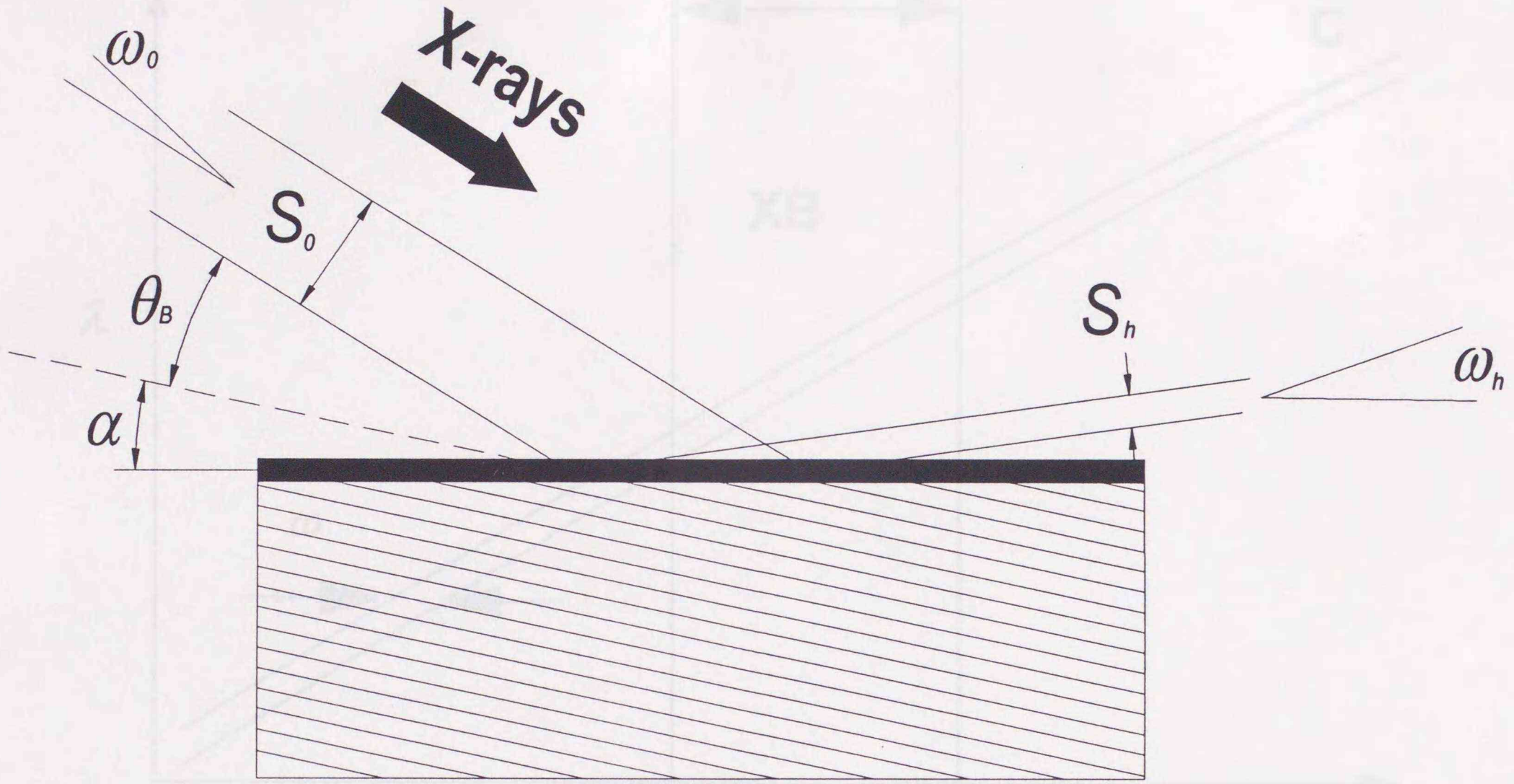


Fig. 33 : Asymmetric monochromator.

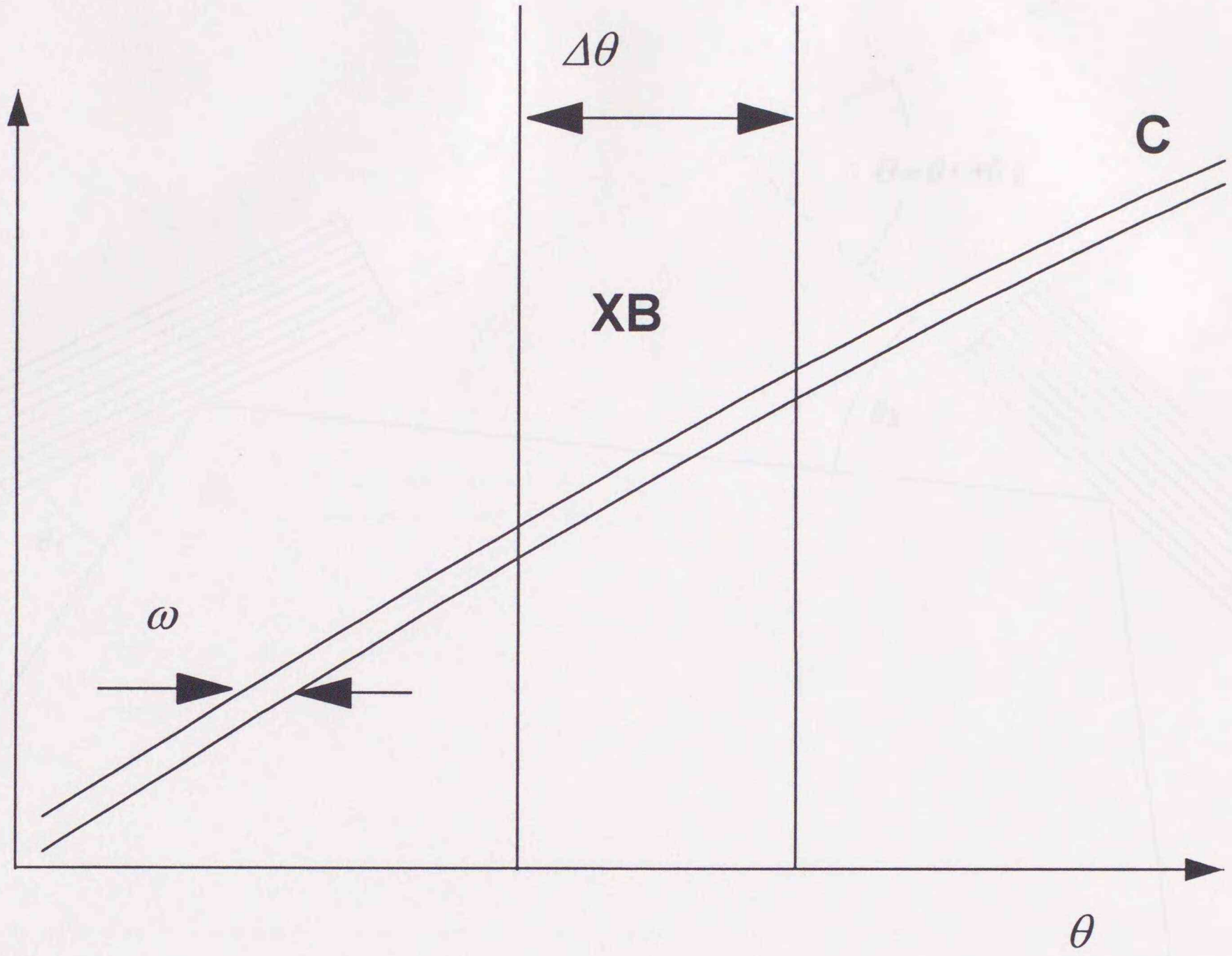


Fig. 34 : DuMond diagram. *C* : monochromator; *XB* : white radiation with angle extension $\Delta\theta$. Only the common part of *C* and *XB* can be reflected by the crystal.

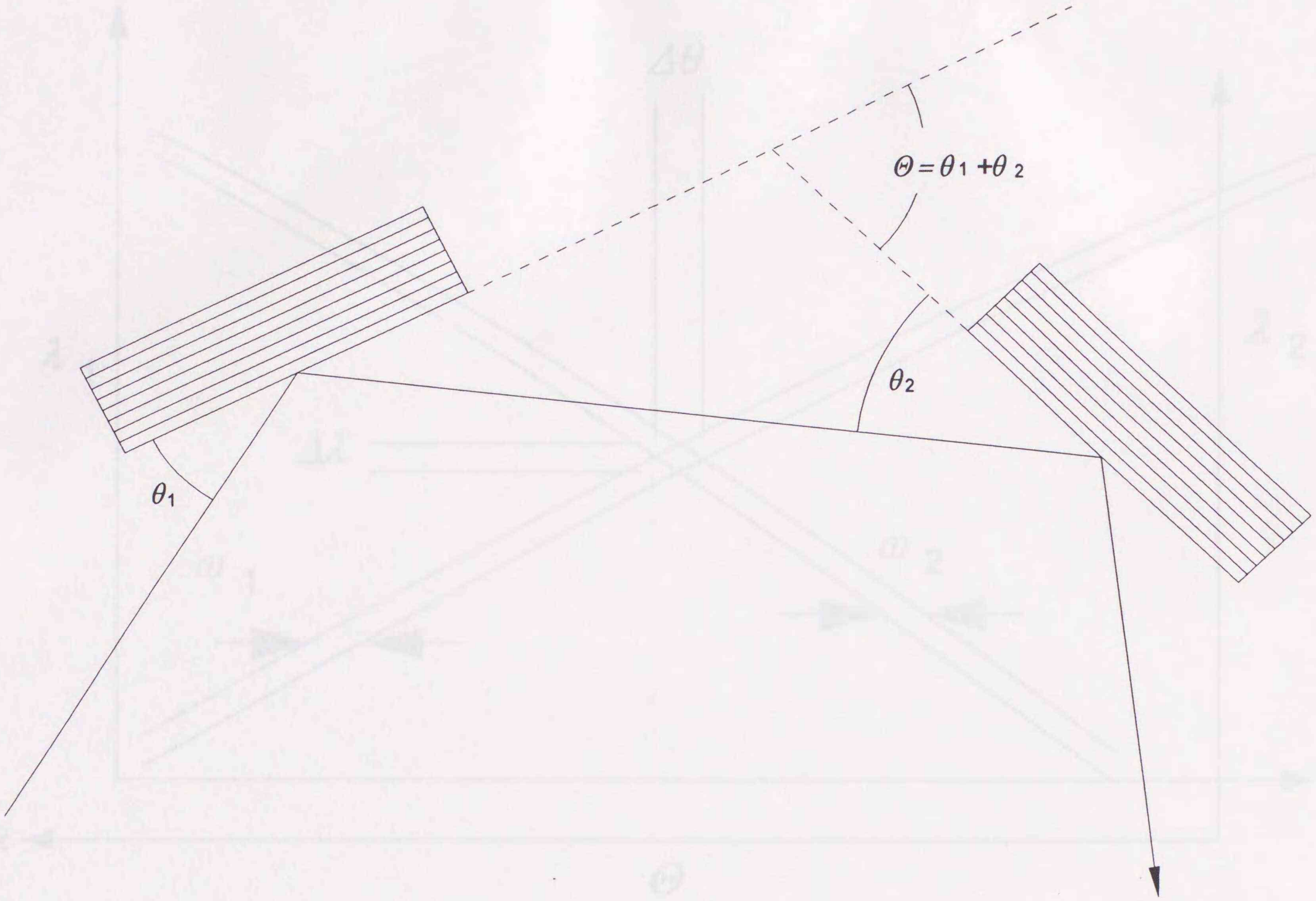


Fig. 35 : (+, +) configuration of symmetry-cut monochromator.

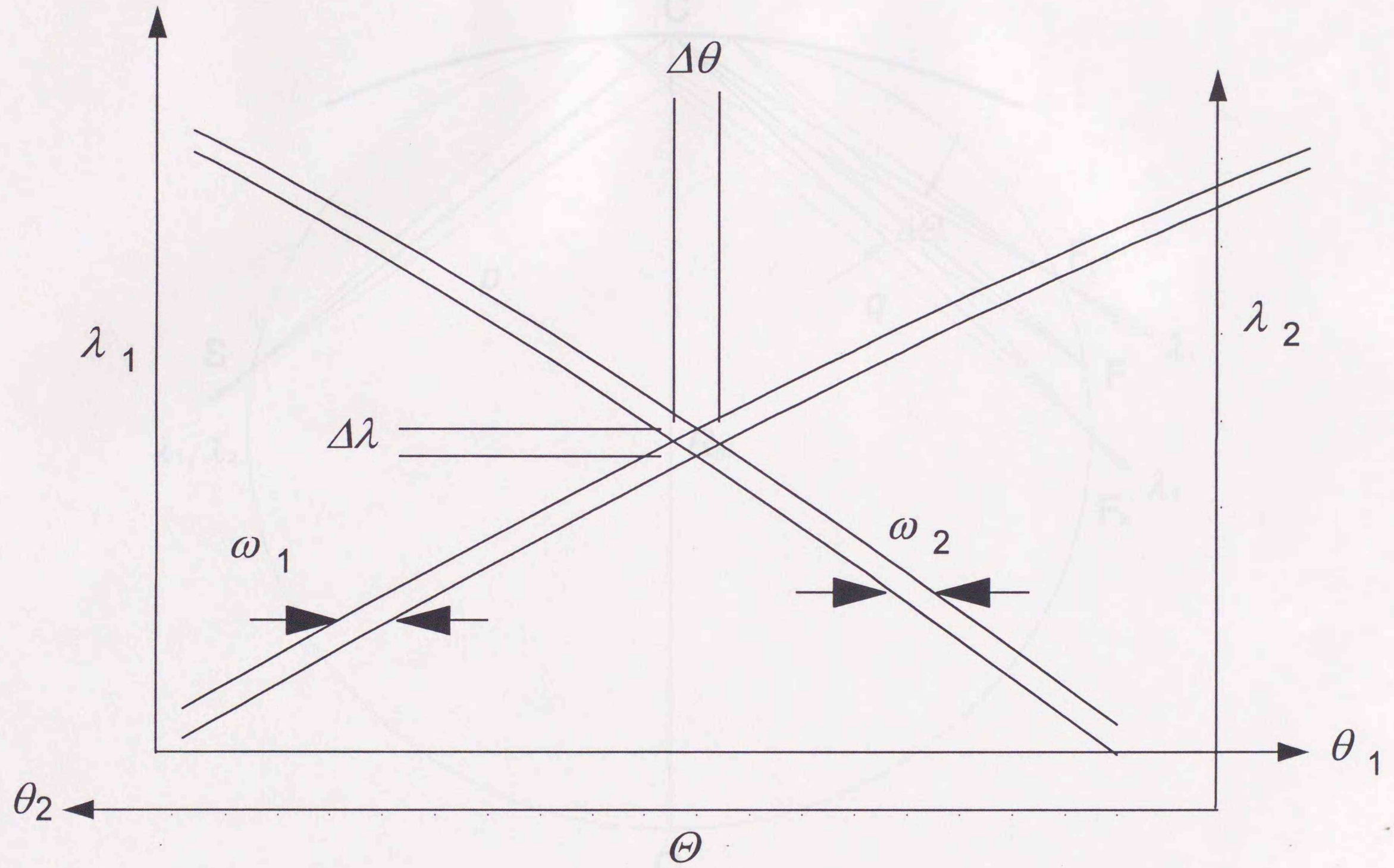


Fig. 36 : DuMond diagram of two monochromators in (+, +) configuration.

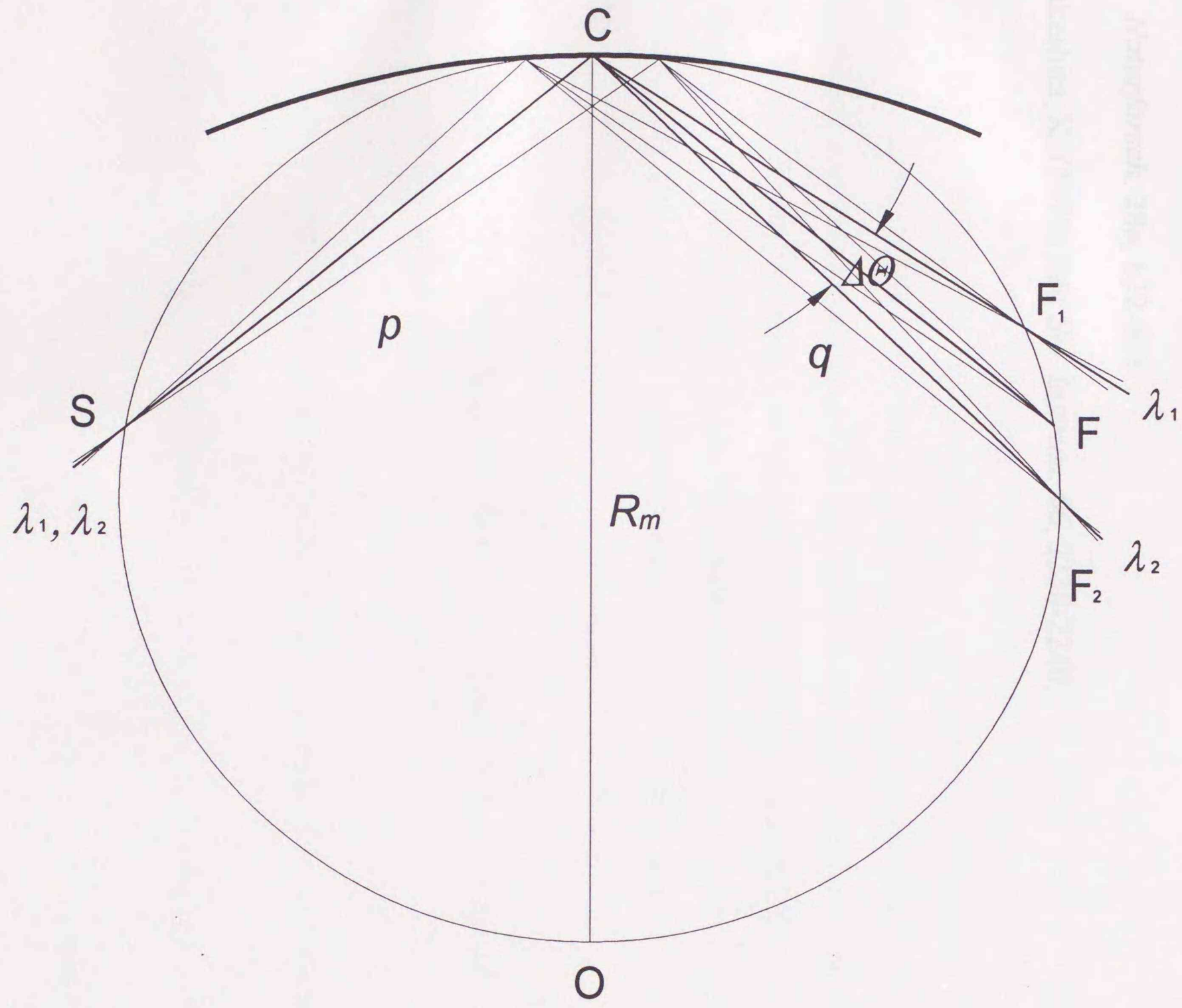


Fig. 37 : Johann-type crystal monochromator. X-rays with wavelengths between $\lambda_2$ and $\lambda_1$ emitted from *S* are reflected from each point of the crystal. X-rays with wavelength $\lambda_1$ focus at $F_1$ and those with wavelength $\lambda_2$ focus at point $F_2$.

# References

DuMond, J. W. M. (1937) *Phys Rev.* **52**, 872-883.

Nakayama, K., Hasizume, H., Miyoshi, A., Kikuta, S. and Kohara, K. (1972) *Z. Naturforsch*. **28a**, 632-638.

Takeshita, K. (1995) *Rev. Sci. Instrum.* **66**, 2238-2240.

# 8. Acknowledgment

I thank to Professor Isao Tanaka who introduced me to the exciting field of protein crystallography.

I acknowledge Drs. Hitoshi Yamaoka and Tomoya Uruga, and Mr. Shigeru Munekawa of RIKEN for their support in experiments. I am also grateful to Dr. Tatsuo Ueki of RIKEN for his encouragement. I also thank the staff of the Photon Factory, in particular, Professor Hiroshi Kawata for useful discussions on the two-dimensional focusing monochromators and Professor Noriyoshi Sakabe for his gift of the BAS-UR imaging plate. I would like to thank Professor Kunio Hikichi for his witty comments and valuable advice. My sincere thanks are due to the members of laboratory for their help and encouragement and to my many friends for their support.

I thank Dr. Nobuo Kamiya of RIKEN whose guidance was invaluable to the completion of this dissertation.

Finally, I would like to thank my family for their understanding and support.

This work was supported by the R&D program of the SPring-8 Project Team.

*January 1996*

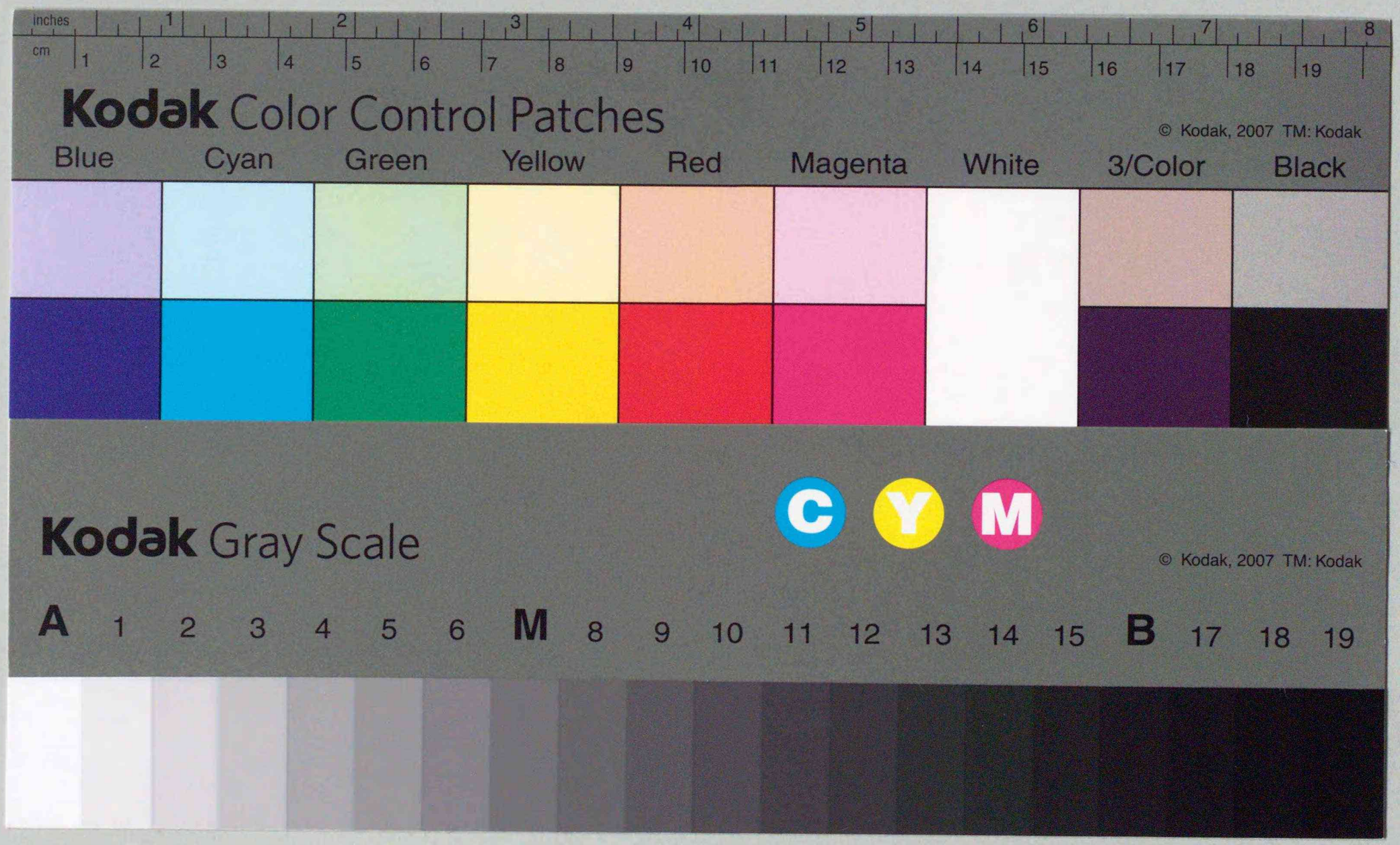
inches
cm
Kodak Color Control Patches
© Kodak, 2007 TM: Kodak
Blue
Cyan
Green
Yellow
Red
Magenta
White
3/Color
Black
Kodak Gray Scale
C
Y
M
© Kodak, 2007 TM: Kodak
A 1 2 3 4 5 6 M 8 9 10 11 12 13 14 15 B 17 18 19